AGU PUBLICATIONS

JGR

Journal of Geophysical Research: Oceans

RESEARCH ARTICLE
10.1002/2016JC011991

Special Section:
The Arctic: An AGU Joint Special Collection

Sea ice algae chlorophyll *a* concentrations derived from under-ice spectral radiation profiling platforms

Benjamin A. Lange[1,2], Christian Katlein[1], Marcel Nicolaus[1], Ilka Peeken[1,3], and Hauke Flores[1,2]

[1]Alfred-Wegener-Institut Helmholtz-Zentrum für Polar-und Meeresforschung, Bremerhaven, Germany, [2]University of Hamburg, Zoological Institute and Zoological Museum, Biocenter Grindel, Hamburg, Germany, [3]MARUM, Center for Marine Environmental Sciences, University of Bremen, Bremen, Germany

Key Points:
- Ice-algal chl *a* concentrations derived from under-ice spectral radiation were best estimated using EOF-approach
- Accounting for variability of incoming solar irradiance produced most reliable ice-algal biomass estimates
- Insufficient spatial representativeness of sea ice-algal biomass can cause biases in large-scale ice-algal biomass and PP estimates

Supporting Information:
- Table S1
- Table S2
- Table S3

Correspondence to:
B. Lange,
benjamin.lange@awi.de

Citation:
Lange, B. A., C. Katlein, M. Nicolaus, I. Peeken, and H. Flores (2016), Sea ice algae chlorophyll *a* concentrations derived from under-ice spectral radiation profiling platforms, *J. Geophys. Res. Oceans*, *121*, doi:10.1002/2016JC011991.

Received 23 MAY 2016
Accepted 11 NOV 2016
Accepted article online 16 NOV 2016

Abstract Multiscale sea ice algae observations are fundamentally important for projecting changes to sea ice ecosystems, as the physical environment continues to change. In this study, we developed upon previously established methodologies for deriving sea ice-algal chlorophyll *a* concentrations (chl *a*) from spectral radiation measurements, and applied these to larger-scale spectral surveys. We conducted four different under-ice spectral measurements: irradiance, radiance, transmittance, and transflectance, and applied three statistical approaches: Empirical Orthogonal Functions (EOF), Normalized Difference Indices (NDI), and multi-NDI. We developed models based on ice core chl *a* and coincident spectral irradiance/transmittance ($N = 49$) and radiance/transflectance ($N = 50$) measurements conducted during two cruises to the central Arctic Ocean in 2011 and 2012. These reference models were ranked based on two criteria: mean robustness R^2 and true prediction error estimates. For estimating the biomass of a large-scale data set, the EOF approach performed better than the NDI, due to its ability to account for the high variability of environmental properties experienced over large areas. Based on robustness and true prediction error, the three most reliable models, EOF-transmittance, EOF-transflectance, and NDI-transmittance, were applied to two remotely operated vehicle (ROV) and two Surface and Under-Ice Trawl (SUIT) spectral radiation surveys. In these larger-scale chl *a* estimates, EOF-transmittance showed the best fit to ice core chl *a*. Application of our most reliable model, EOF-transmittance, to an 85 m horizontal ROV transect revealed large differences compared to published biomass estimates from the same site with important implications for projections of Arctic-wide ice-algal biomass and primary production.

1. Introduction

Many of the most pronounced changes in the Arctic Ocean have been observed in the physical sea ice environment, as these properties are easily monitored and up-scaled using satellites and air-borne sensors. Such changes include: dramatic reductions in sea ice extent [*Serreze et al*., 2007; *Stroeve et al*., 2012] and thickness [*Haas et al*., 2008; *Kwok and Rothrock*, 2009]; replacement of multiyear ice (MYI) by first-year ice (FYI) [*Maslanik et al*., 2011]; increased light transmittance through the summer sea ice cover [*Nicolaus et al*., 2012], decreased summer sea ice albedo [*Riihelä et al*., 2013]; and increased melt-pond coverage [*Rösel and Kaleschke*, 2012]. These changes to the Arctic sea ice cover are likely to continue unabated into the future, having profound ecological consequences [Arctic Monitoring and Assessment Programme (*AMAP*), 2011; Intergovernmental Panel on Climate Change (*IPCC*), 2013].

Satellite observations have already indicated increased pelagic production within the Arctic Ocean due to decreased ice cover and a longer open water season [*Arrigo et al*., 2008; *Arrigo and van Dijken*, 2011]. A recent study in the Central Arctic Ocean also suggested that sea ice-related primary production has increased and will continue to increase in the Central Arctic due to more light penetrating through the ice [*Fernández-Méndez et al*., 2015]. However, many other variables are likely to have an equal or greater influence on primary production than light alone, such as: nutrient supply, temperature and CO_2 intake by the Arctic Ocean [*Tremblay et al*., 2015]. Increased CO_2 intake by the Ocean due to less sea ice may increase PP but this could also be counteracted by higher temperatures and increased runoff [*Tremblay et al*., 2015]. Furthermore, increased freshwater input may result in lower primary production due to less available nutrients [*Yun et al*., 2016].

Changes to ice-associated production, however, are even more difficult to evaluate due to a lack of studies in the Central Arctic [*Wassmann et al*., 2011]. Monitoring sea ice ecosystems remains a challenge due to logistical constraints and the difficulty of remotely sensing biological processes in and under the ice cover [*Wassmann et al*., 2011]. As sea ice algae are a major source of energy for many key marine organisms in the Arctic [*Budge et al*., 2008; *Kohlbach et al*., 2016; *Søreide et al*., 2013; *Wang et al*., 2015], sea ice algae observations conducted at different spatial scales (i.e., a few meters, hundreds of meters, a few kilometers, and hundreds of kilometers) are of particular interest in order to address potential changes to the sea ice ecosystem as the physical environment continues to change.

There is growing interest in extending sea ice-algal observations by developing larger-scale observation systems and methodologies that can capture the spatial distribution of sea ice algae at multiple scales. Although sea ice coring will remain an essential method for any ice-related research, point measurement coring is time consuming, making it an unlikely candidate for large-scale ice-algal observation systems. Other devices such as the slurp-gun [*Gosselin et al*., 1990] or underwater pulse-amplitude-modulated fluorometer (Diving-PAM) [*Rysgaard et al*., 2001] have shown promise, however, they require the deployment by divers, which is logistically demanding, time intensive and often not possible due to security reasons.

New developments of Autonomous Underwater and Remotely Operated Vehicles (AUV/ROV) give promising new opportunities to study the underside of ice [*Wadhams*, 2012]. Currently these platforms have mainly been used to observe physical [e.g., *Katlein et al*., 2015; *Nicolaus and Katlein*, 2013; *Nicolaus et al*., 2012; *Wadhams*, 2012] and biological [e.g., *Ambrose et al*., 2005; *Katlein et al*., 2014a] processes within and under the ice at scales of 10–500 m, and with relatively minimal logistical requirements, in terms of spatial coverage compared to other methods (e.g., 8 h for 100–500 m transects). ROVs deployed with mounted digital imagery systems have been used to document the distribution of subice-algal aggregates [e.g., *Ambrose et al*., 2005; *Gutt*, 1995; *Katlein et al*., 2014a]. Digital imagery is limited to two-dimensional space and therefore abundance estimates may have high uncertainty. Using image analysis, *Katlein et al*. [2014a] showed that ice-algal aggregate distribution is mainly controlled by under-ice topography with the accumulation of aggregates along the edges of ridges and in dome-shaped ice features.

Under-ice spectral radiation measurements can be used to derive chlorophyll *a* concentrations in sea ice using bio-optical models. Until now, however, these models have not been applied to larger scale under-ice ROV spectral radiation measurements. ROVs have recently been deployed, with mounted spectral radiometers, to measure under-ice spectral irradiance [e.g., *Katlein et al*., 2015; *Katlein et al*., 2014b; *Nicolaus and Katlein*, 2013; *Nicolaus et al*., 2012]. Spectral radiometers have also been mounted on Surface and Under-Ice Trawls (SUIT) [*van Franeker et al*., 2009], a potential horizontal profiling platform for monitoring ice-algal concentration in combination with the abundance of under-ice grazers over profiles up to 3 km in length [e.g., *David et al*., 2015]. The development of under-ice horizontal profiling platforms for observing spectral properties of sea ice, among other properties, has resulted in and will continue to result in larger amounts of under-ice spectra. These spectral observations, both from the past and future, could be used to estimate the temporal evolution and spatial variability of ice-algal chl *a*. However, this requires the development of robust and reliable methodologies that can be applied to data sets with variable temporal and spatial coverage, and with a large range of environmental conditions.

Sea ice-algal chl *a* concentrations derived from under-ice spectral radiation have been estimated using a normalized difference index method (NDI), introduced by *Mundy et al*. [2007] and applied in other field studies [e.g., *Campbell et al*., 2014]. This method has proved useful during springtime to detect under-ice spectral variations near the 440 nm chl *a* absorption peak in order to estimate bottom ice chl *a* concentrations. Their NDI-derived chl *a* concentrations agreed well with chl *a* estimates from ice core samples. The second chl *a* absorption peek at ~670 nm, however, did not provide an accurate bio-optical model due to the stronger influence of snow in the same wavelength range [*Mundy et al*., 2007].

Alternatively, Empirical Orthogonal Function (EOF) analysis has been used to identify variations within underwater spectral radiation measurements and estimate water column concentrations of chl *a* [*Craig et al*., 2012] and phycoerythrin [*Taylor et al*., 2013]. *Melbourne-Thomas et al*. [2015] compared several statistical approaches, including: NDI, EOF, ratios of spectral irradiance, and scaled band area, to estimate ice-algal biomass from under-ice spectra measured during winter and spring expeditions in the ice-covered Southern Ocean. Their results indicated that the NDI method was most robust for their data set, but the EOF also

provided reliable model results. In these previous studies, they only used point measurements to test the reliability of the models.

Previous work on deriving concentrations of chl *a* and pigments from spectral radiation measurements have demonstrated essential methodological advancements and applications [*Campbell et al*., 2014, 2015; *Craig et al*., 2012; *McDonald et al*., 2015; *Melbourne-Thomas et al*., 2015; *Mundy et al*., 2007; *Taylor et al*., 2013]. The application of ice-algal chl *a* estimates derived from under-ice spectral radiation, however, remains limited to local point measurements, with limited spatial coverage, and limited to a time period when the snow cover dominates the influence of light attenuation. This period is also when ice algae have highest biomass levels for these corresponding low-latitude ($\sim<80°$N) regions characterized by seasonal sea ice [*Leu et al*., 2015]. At higher latitudes of the central Arctic Ocean, however, ice-algal biomass peaks have been reported during later stages of summer when snow is absent [*Melnikov*, 1997; *Melnikov et al*., 2002]. Furthermore, during spring the transmittance of light through sea ice is largely influenced by snow depth [*Hamre et al*., 2004; *Järvinen and Leppäranta*, 2011; *Maykut and Grenfell*, 1975; *Thomas*, 1963] and to a lesser extent sea ice thickness [*Grenfell and Maykut*, 1977; *Light et al*., 2008; *Nicolaus et al*., 2010a; *Thomas*, 1963]. Therefore, the initial spring growth of sea ice-algal communities is typically controlled by snow depth due to its larger influence on light transmittance [*Campbell et al*., 2015; *Gosselin et al*., 1986; *Mundy et al*., 2007]. During summer when snow is absent, light transmittance through sea ice is greater and is largely controlled by variability of the sea ice properties [e.g., melt ponds versus bar ice; *Light et al*., 2008; *Nicolaus et al*., 2012; *Perovich*, 1996]. In the absence of snow and the onset of melt, algal communities shift to a nutrient limited system and are expelled from the ice during advanced and rapid melt [*Cota and Smith*, 1991; *Gosselin et al*., 1990; *Lavoie et al*., 2005].

Previous work deriving ice-algal chl*a* estimates from under-ice spectral radiation has focused on under-ice irradiance, which does not account for variations of the incoming solar radiation. Variability of incoming radiation and more importantly variations of the solar elevation angle not only produce variations in magnitude but also variations in spectral shape, which may introduce variability (i.e., artificial chl *a* absorption signals) within spectral regions of maximum chl *a* absorption. Furthermore, the observed snow and sea ice albedos, and subsequently the attenuation of light within the snow and sea ice can be drastically different for the same snow and ice depending on the incident solar radiation conditions (e.g., clear skies versus cloud cover) [*Grenfell and Maykut*, 1977; *Perovich*, 1996].

The main motivation for this work is to find a reliable bio-optical model for estimating the variability of ice-algal chl *a* under highly heterogeneous environmental conditions that can be applied to larger scale spectral measurements using under-ice horizontal profiling platforms (e.g., ROV and SUIT). We accomplished this by developing upon previously established bio-optical methodologies and statistical approaches. We determined the best ranked bio-optical model for estimating ice-algal biomass by comparing: (i) different statistical approaches: NDI and EOF, including a newly introduced multi-NDI method that takes advantage of both chl *a* absorption peaks; and (ii) different spectral measurements, including: under-ice irradiance, under-ice radiance, under-ice transmittance and under-ice transflectance. We applied a selected most reliable set of models to larger scale spectral surveys for additional model assessment and comparison. In addition, we provided a preliminary analysis of the spatial distribution of ice algae based on a short transect extracted from a selected ROV survey.

2. Materials and Methods

2.1. Study Area

Field observations and sampling for this study were conducted during two summer research cruises to the Central Arctic Ocean onboard the German icebreaker R/V *Polarstern*: (i) *TransArc* (PS78.3, hereafter referred to as PS78) conducted from 4 August to 7 October 2011 (Figure 1); and (ii) *IceArc* (PS80.3, hereafter referred to as PS80) conducted from 4 August to 8 October 2012 (Figure 1). Measurements and ice core samples were acquired from a total of six ice stations during the PS78 cruise, and from nine ice stations, one helicopter ice landing and two Surface and Under-Ice Trawl profiles (SUIT; with mounted sensor array) during the PS80 cruise.

2.2. Spectral Measurements

Spectral radiance and irradiance measurements were acquired using Ramses spectral radiometers (Trios GmbH, Rastede, Germany) with a wavelength range from 350 to 920 nm and a resolution of 3.3 nm, which

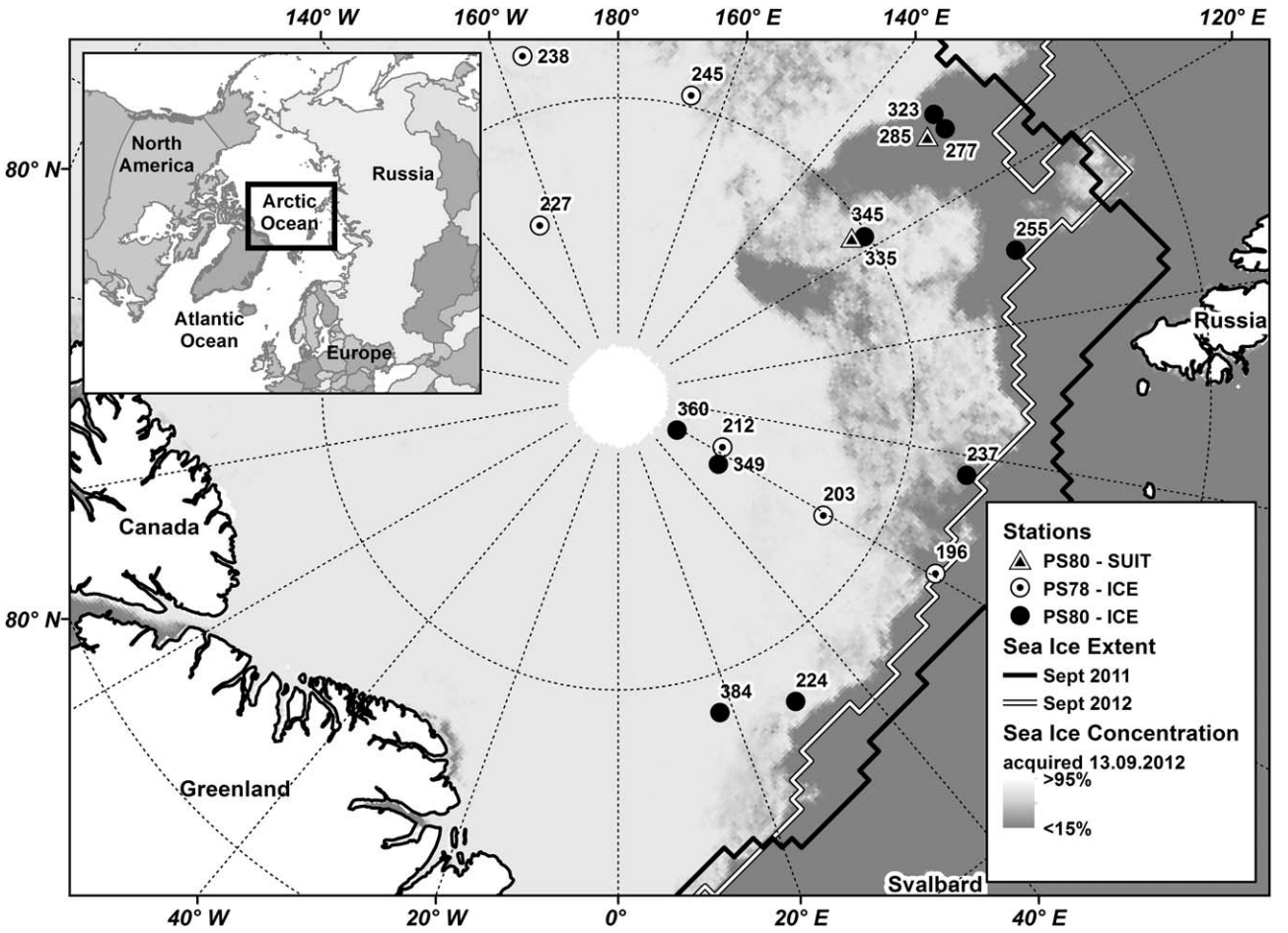

Figure 1. Map of the study region with ice stations conducted during expeditions PS78 and PS80, and the two selected SUIT sampling sites. Sea ice concentration data acquired from www.meereisportal.de according to algorithms in *Spreen et al.* [2008]. Sea ice extent corresponds to monthly means during September for both cruise years [extent data acquired from NSIDC; *Fetterer et al.*, 2002, udpated 2011].

were subsequently interpolated to a 1 nm grid following *Nicolaus et al.* [2010b]. Incident solar radiation (E_S) and under-ice irradiance (E_T) were measured using an irradiance sensor (RAMSES-ACC) containing a cosine receptor with a180° field-of-view (FOV. Under-ice radiance (I_T) measurements were acquired using a radiance sensor (RAMSES-ARC) with a 9° FOV. According to *Nicolaus et al.* [2010b] and *Katlein et al.* [2014b], the effective measurement footprint diameter for the irradiance sensor, f_i, was calculated as:

$$f_i = 2d \tag{1}$$

where d is the distance to the ice bottom, and the footprint diameter for the radiance sensor, f_r, was calculated as:

$$f_r = 2d \ \tan 4.5^\circ \tag{2}$$

All spectral measurements are presented for the photosynthetically active radiation range (PAR) between 400 and 700 nm, unless stated otherwise. Additional details about the sensors and spectral data processing were described by *Nicolaus et al.* [2010b]. Spectral transmittance (T_E) is defined as the ratio of under-ice irradiance (E_T) to incident solar radiation (E_S), as described by *Nicolaus et al.* [2010b]:

$$T_E(\lambda) = \frac{E_T(\lambda)}{E_s(\lambda)} \tag{3}$$

with wavelength λ within the PAR range (400:700 nm). Spectral transflectance (T_I), introduced by *Nicolaus and Katlein* [2013], is defined as the ratio of under-ice radiance (I_T) to incident solar radiation (E_S):

$$T_I(\lambda) = \frac{I_T(\lambda)}{E_s(\lambda)} \quad (4)$$

Transmittance and transflectance are dimensionless, however, following the SI-system to use steradian for solid angles, we use sr^{-1} as the unit for transflectance following *Nicolaus and Katlein* [2013].

Under-ice spectral radiation measurements were conducted using: (i) an under-ice L-arm sensor system; (ii) a remotely operated vehicle (ROV), V8Sii-ROV (Ocean Modules, Åtvidaberg, Sweden), with mounted sensor array; and (iii) a Surface and Under Ice Trawl (SUIT) [*van Franeker et al*., 2009] with mounted sensor array, as described by *David et al*. [2015]. Simplified diagrams and images showing the deployment of all under-ice profiling platforms are presented in Figure 2. The under-ice L-arm sensor system (Figures 2a and 2e), previously described in *Melbourne-Thomas et al*. [2015] and *Mundy et al*. [2007], was deployed below the ice through a ~14 cm diameter vertical hole drilled using a Kovacs Mark II 9 cm internal diameter corer (Kovacs Enterprise, Roseburg, USA). Once the L-arm was below the ice, the lower ~1.2 m of the aluminum bar setup, with mounted radiometer (e.g., irradiance or radiance sensor), was extended horizontally, and then slowly raised so the sensor was ~10 cm from the ice bottom. To minimize shading by the system equipment and operator, the sensor was positioned directly south of the L-arm hole at ~1.2 m distance. Coincident incoming irradiance measurements were conducted above the ice for all under-ice L-arm measurements. The snow/ice surface directly south of the L-arm hole was kept undisturbed during spectral measurements. Ice cores were then sampled after the spectral measurements at the same locations (see section 2.3; and Figures 2a and 2b).

A detailed description of the ROV (Figures 2c and 2f) spectral measurements, calibration and calculations, and ROV operation during PS78 was provided by *Nicolaus and Katlein* [2013]. The V8ii ROV was equipped with an altimeter (DST Micron Echosounder, Tritech, UK), a sonar (Micron DST MK2, Tritech, UK), one zoom-camera (Typhoon, Tritech, UK), and one fixed focal length camera (Ospray, Tritech, UK). In addition, the ROV system had a built-in set of internal sensors such as: magnetic and three-axes gyro compass, three-axes accelerometer, and a pressure sensor. Some minor modifications to the ROV system were made for the PS80 cruise and are described in *Katlein et al*. [2014a]. ROV spectral measurements, calibration, and calculations during PS80 were consistent to those used during PS78 and conducted as described in *Nicolaus and Katlein* [2013]. Under-ice ROV spectral surveys (Figure 2a) were performed over perpendicular *x*-*y* transects with *x* and *y* transect lengths between 50 and 150 m. Incident solar radiation (E_S) measurements, for the calculation of spectral transmittance and transflectance, were performed using an irradiance sensor mounted on a tripod positioned on the sea ice nearby the ROV operation tent (Figure 2a). Stationary spectral measurements were conducted directly (~0–10 cm) under the ice at 10 m intervals along the *x*-*y* transects. When the ROV spectral surveys were complete, ice cores were extracted at predetermined locations along the ROV transects at the same location of selected spectral measurements (Figure 2a).

The Surface and Under Ice Trawl (SUIT) [*van Franeker et al*., 2009] is a net used to sample sea ice fauna, zooplankton and micronekton in the upper 2 m of the water column under the ice (Figures 2d, 2g, and 2h). A detailed description of the SUIT is provided as supporting information in *Flores et al*. [2012]. During PS80 the sensor array was specifically enhanced with the aim to measure the variability of sea ice algae within the sea ice along the SUIT hauls. The new sensor package included an Acoustic Doppler Current Profiler (ADCP), a Conductivity Temperature Depth probe (CTD) with built-in fluorometer, an altimeter, one irradiance sensor (RAMSES-ACC), one radiance sensor (RAMSES-ARC) and a forward-looking video camera (Figure 2h; previously described in *David et al*. [2015]). The sensor array provides measurements of under-ice spectral radiation, and pitch, roll, depth, and distance to ice-bottom, which were used to calculate ice draft.

2.3. Spectral Quality Control of Under-Ice Profiling Platforms

SUIT and ROV covered different distances and were operated at various depths under the ice along the profiles. Therefore, the data needed to be filtered to get suitable spectra for the bio-optical prediction models. Pitch and roll, and distance to ice bottom measurements were used to filter the spectra in order to minimize the influence of light attenuation by water. The integration time of the spectral radiometers varied with the strength of the received radiation, which was highly variable under sea ice. Therefore, ADCP measurements (1 Hz) and distance to ice (10 Hz) were averaged over the integration time interval of each spectral measurement. The footprint of each measurement was dependent on the distance to the ice bottom, the field-

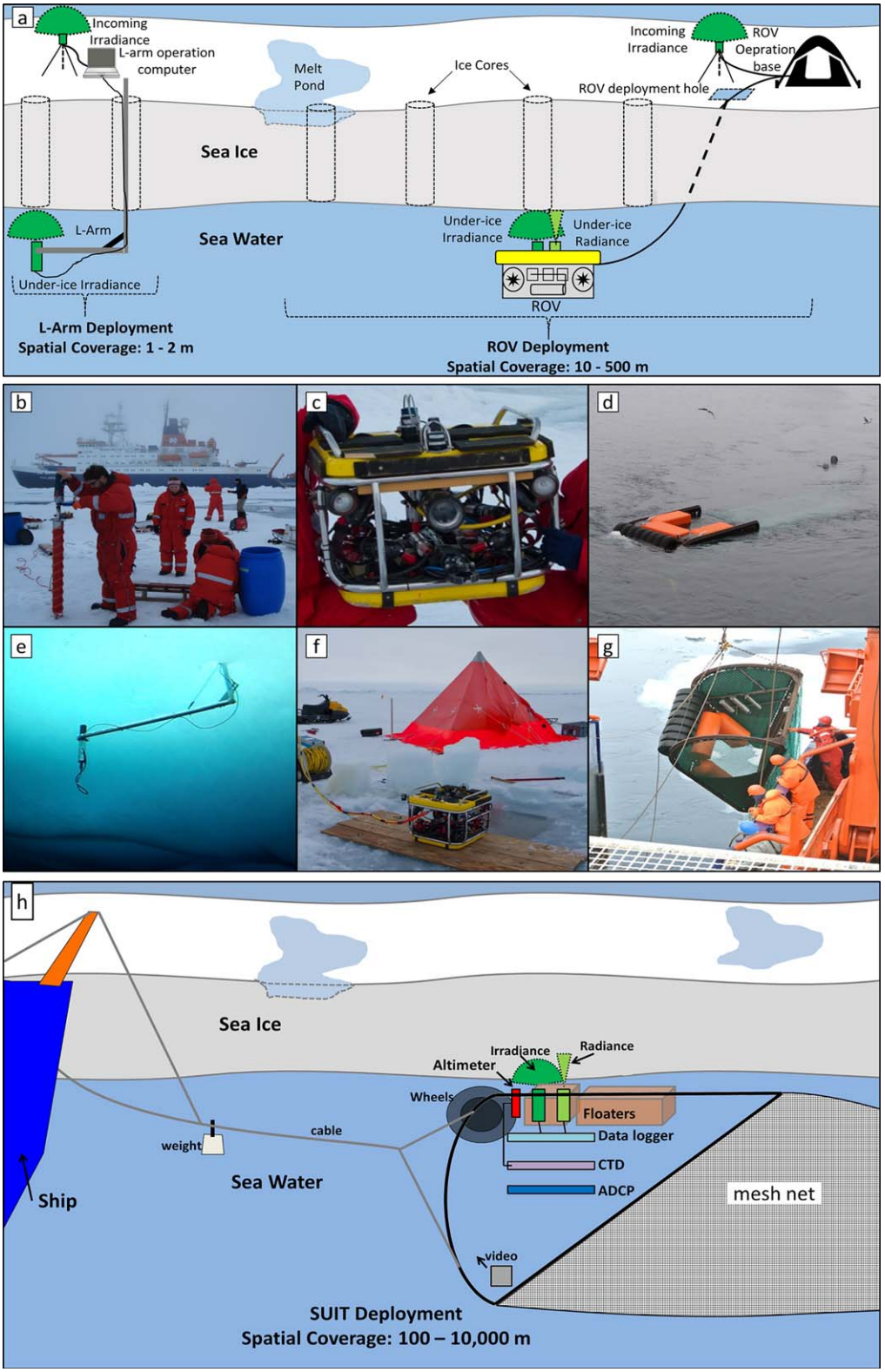

Figure 2. Diagrams and images showing under-ice horizontal spectral profiling platforms and sea ice sampling. (a) shows ice station work, e.g., deployment of the L-arm and remotely operated vehicle (ROV), and ice core extraction; (b) shows ice coring; (c) the ROV; (d) the surface and under-ice trawl (SUIT) floating in the water; (e) the L-arm deployed under the ice with a mounted radiance sensor; (f) the ROV adjacent to the deployment hole and operation tent; (g) the SUIT being lifted back onto Polarstern, with sensor array on portside wing; and (h) the SUIT, with mounted sensor array, being towed behind a ship. Note: (a) and (h) are not to scale.

Table 1. Summary of Environmental Properties and Bio-Optical Cores for Each Ice Station

Cruise/ Station	Ice Station[a]	Date (dd/mm/yy)	Latitude	Longitude	Ice Type	SIC[b]	Modal Ice Thickness[b]	$E_{S\ (PAR)}$[c]	$E_{T\ (PAR)}$[c]	$T_{E\ (PAR)}$[d]	$I_{T\ (PAR)}$[c]	$T_{I\ (PAR)}$[d]	N	Core Length (m)	Snow (m)	Scatt. (m)	mg chl a m^{-2}
PS78/196	Ice-1	11 Aug 2011	83.84	60.50	FYI			53.9	2.8	0.05			1	0.90	0.00	0.05	0.17
PS78/203	Ice-2	14 Aug 2011	85.97	59.35	NEW			37.0		0.06			1	0.05			0.05
PS78/212	Ice-4	19 Aug 2011	88.02	59.45	FYI		1.2	35.5 ± 5.8	14.0 ± 6.3	0.29 ± 0.2			3	0.93 ± 0.20			0.57 ± 0.27
PS78/227	Ice-7	29 Aug 2011	86.86	−155.05	FYI		1.1	18.6 ± 4.4	1.7 ± 1.8	0.10 ± 0.11	1.1 ± 0.8	0.07 ± 0.05	3	1.92 ± 1.43	0.00	0.02 ± 0.02	0.18 ± 0.18
PS78/239	Ice-10	06 Sep 2011	84.072	−164.19	MYI		0.8	42.8 ± 11.9	1.4 ± 0.9	0.03 ± 0.02	0.6 ± 0.6	0.01 ± 0.01	3	1.64 ± 0.79			0.40 ± 0.27
PS78/245	Ice-11	08 Sep 2011	84.81	166.22	FYI		1.2	39.3 ± 16.7	1.0 ± 0.1	0.04 ± 0.03	0.8 ± 0.6	0.02 ± 0.02	3	0.82 ± 0.62			0.17 ± 0.15
PS80/224	Ice-1	10 Aug 2012	84.00	30.00	FYI	80	1.0	50.7 ± 2.1			2.4 ± 2.2	0.04 ± 0.04	8	1.33 ± 0.41	0.00	0.09 ± 0.17	0.38 ± 0.22
PS80/237	Ice-2	15 Aug 2012	83.95	76.85	FYI	80	1.3	77.7 ± 10.6	5.2 ± 7.6	0.07 ± 0.11	3.6 ± 4.2	0.04 ± 0.05	12	1.54 ± 0.55	0.00	0.04 ± 0.03	0.82 ± 0.58
PS80/255	Ice-3	20 Aug 2012	82.86	109.86	FYI	70	0.9	35.0 ± 1.4	4.7 ± 0.5	0.13 ± 0.01	2.4 ± 0.5	0.06 ± 0.01	4	0.76 ± 0.17	0.00	0.03 ± 0.02	1.03 ± 0.66
PS80/277	Ice-4	26 Aug 2012	82.89	129.78	FYI	80							5	0.63 ± 0.29	0.00	0.03 ± 0.04	0.19 ± 0.20
PS80/323	Ice-5	05 Sep 2012	82.88	130.76	FYI	60	0.8	91.4 ± 9.1	2.9 ± 0.6	0.04 ± 0.02	1.6 ± 0.5	0.02 ± 0.02	6	0.73 ± 0.58	0.04 ± 0.02	0.00	0.16 ± 0.13
PS80/335	Ice-6	08 Sep 2012	85.06	122.52	FYI	50	0.7	69.2 ± 8.4	2.7 ± 2.4	0.03 ± 0.03	1.4 ± 1.7	0.02 ± 0.02	6	1.07 ± 0.49	0.07 ± 0.07	0.00	0.96 ± 0.91
PS80/349	Ice-7	19 Sep 2012	87.93	60.95	MYI	100	1.6	14.4 ± 1.3	1.0 ± 1.0	0.09 ± 0.09	0.8 ± 0.8	0.05 ± 0.06	7	0.89 ± 0.56	0.01 ± 0.01	0.00	1.62 ± 2.09
PS80/360	Ice-8	22 Sep 2012	88.83	58.53	MYI	100	1.8	8.0 ± 0.5	0.2 ± 0.1	0.02 ± 0.01	0.2 ± 0.1	0.01 ± 0.01	4	1.11 ± 0.36	0.04 ± 0.03	0.00	6.59 ± 4.91
PS80/384	Ice-9	29 Sep 2012	84.35	17.73	FYI	100	1.2	9.9 ± 0.5	0.2 ± 0.1	0.02 ± 0.02	0.1 ± 0.0	0.01 ± 0.01	4	1.07 ± 0.65	0.04 ± 0.02	0.00	0.40 ± 0.49
PS80/HELI-64		27 Sep 2012			NEW			23.1 ± 2.7		0.54 ± 0.09		0.25 ± 0.02	3	0.05 ± 0.01	0.00 ± 0.00	0.00	0.03 ± 0.01

Latitude are in degrees North; negative longitude are degrees West and positive longitude are degrees East. NEW refers to newly formed sea ice. SIC is sea ice concentration. E_S is incident solar radiation; E_T is under-ice irradiance; T_E is spectral transmittance; I_T is under-ice radiance; T_I is spectral transflectance. Scatt. is the scattering surface layer depth.

[a]Added for easy cross reference to other publications using this naming protocol [e.g., *Boetius et al*., 2013; *Fernández-Méndez et al*., 2015; *Katlein et al*., 2014a]

[b]Data presented in *Nicolaus and Katlein* [2013] for PS78 and *Katlein et al*. [2014a] for PS80.

[c]$E_{S\ (PAR)}$ incident solar radiation; $E_{T\ (PAR)}$ under-ice irradiance; and $I_{T\ (PAR)}$ under-ice radiance were integrated over PAR wavelengths 400–700 nm.

[d]$T_{E\ (PAR)}$ spectral transmittance; and $T_{I\ (PAR)}$ spectral transflectance are mean over PAR. "-"represent no data.

of-view (FOV) of the sensor (equations (1) and (2)), and the horizontal speed of the sensor platform. Highest quality spectra were acquired when the ROV operated at a constant depth [*Nicolaus and Katlein*, 2013]. However, variations of distance to ice and orientation of the ROV are difficult to minimize and therefore the measurement footprints during ROV surveys were highly variable. We minimized the influence of light attenuation by water on the spectral signal and limited variability of the footprint size by selecting only measurements that had a distance to the ice bottom of $<$1.5 m, and pitch and roll between $-10°$ and $+10°$ [*Nicolaus and Katlein*, 2013]. Due to the diffuse light field, tilt errors were considered not critical, particularly when including a minimum distance threshold of 1.5 m. Similar to the ROV, SUIT haul measurements were also filtered by a distance to ice bottom of $<$1.5 m, and pitch and roll between $-15°$ and $+15°$. Corrections were not applied because they would have introduced errors of unknown size. Under-ice water chl *a* concentrations during our sampling period were low, 0.06–0.24 mg m^{-3} [*David et al*., 2015]. Based on the maximum water chl *a* concentration of 0.24 mg m^{-3} and the maximum distance to ice bottom of 1.5 m, this is equivalent to 0.36 mg chl *a* m^{-2}. This value is slightly larger than some ice core chl *a* concentrations (Table 1), however, it does represent the maximum uncertainty and is overall much lower because the ROV operation distances to ice bottom were predominantly under 1 m and water column chl *a* were typically less than 0.24 mg m^{-3}. Therefore, we assumed minimal influence on the spectral signal by the water chl *a*. Because the ROV was operated at slow speeds ($<$0.2 m s^{-1}) the footprint size had minimal horizontal variability due to movement (e.g., across-track and along-track spatial footprint were equal). The faster horizontal operation speeds of the SUIT ($\sim$1.5 m s^{-1}), however, resulted in an along-track spatial footprint dependent on the integration time of the sensor. Footprint size variability was accounted for by using the footprint as a weighting factor when conducting statistical analyses.

2.4. Ice Coring and Chlorophyll *a* Measurements

A total of 73 sea ice cores were extracted from 16 ice stations using a 9 cm inner diameter ice corer powered by an electric drill. At each core location, we measured snow depth or surface scattering layer depth, ice thickness, core length, and freeboard. Here the scattering layer is defined as an unconsolidated surface layer of large ice granules (~1–5 mm). Ice cores were placed in acid-cleaned barrels, and then immediately transported to the ship and melted at 4°C in the dark. During PS78, ice cores were cut in three parts (the upper and lower 20 cm, and the remaining middle part of the core), placed in separate barrels and processed separately (i.e., three samples for each core). During PS80, each entire ice core was placed in one acid-cleaned barrel for melting and processing (i.e., one sample for each core). Previous comparisons have shown a minor influence on the determination of chl *a* concentrations without the addition of melted sea water [*Miller et al*., 2015; *Rintala et al*., 2014]. When extracting cores from melt ponds, melt-pond water was added to the sample with a volume approximately equal to a 9 cm diameter cylinder (e.g., core barrel) with a height equal to the depth of the melt pond.

Subsamples from each melted sample were filtered onto 25 mm Whatmann GF/F filters, placed in liquid nitrogen then stored in a −80°C freezer until analyses were conducted back at the laboratory in Bremerhaven, Germany. Chl *a* concentrations were measured on each filter using high-performance liquid chromatography (HPLC) as described in *Tran et al*. [2013]. All chl *a* concentrations are reported as vertically integrated units (mg chl *a* m^{-2}).

2.5. Statistical Methods and Approaches

All statistical analyses were conducted using R software Version 2.15.2 [*R-Development-Core-Team*, 2012] with all relevant packages listed after the corresponding analysis description.

2.5.1. Empirical Orthogonal Function (EOF)

The large dimensionality of spectral data (i.e., 301 wavelengths) was reduced by applying Empirical Orthogonal Function (EOF) analyses (also referred to as principal component analyses—PCA). Each spectrum was first standardized by subtracting the mean of the spectrum then dividing by the standard deviation of the spectrum [*Taylor et al*., 2013]. Standardizing the spectra minimizes any variability due to magnitude and allows for a more detailed examination of spectral shape [*Craig et al*., 2012; *Taylor et al*., 2013]. The resulting standardized spectra formed an $N \times M$ matrix X consisting of N observations and M wavelengths = 301 (PAR: 400–700 nm, 1 nm resolution). Using the "*R*" function *cov*, a covariance matrix C was calculated from X:

$$C = \frac{1}{N} X^{T} X \tag{5}$$

We then used the "*R*" function *eigen*, to conduct an eigen decomposition of the covariance matrix C:

$$C = S \Lambda S^{T} \tag{6}$$

where S ($N \times N$) eigenvectors, hereafter referred to as EOFs, contains the loadings for each sample (N) by mode (N). Λ (diagonal matrix with dimensions N) contains the eigenvalues, which explain the variance of each EOF mode. The first EOF mode, captures the largest proportion of variability within the spectra, with each subsequent mode capturing progressively less of the variability. Each selected EOF mode can be represented as a mode of oscillation in the data (spectra) by calculating the EOF expansion coefficients Z. Z was calculated by projecting the spectral matrix X onto S:

$$Z = XS \tag{7}$$

where Z ($M \times N$) contains the loadings for each wavelength (M) by mode (N).

To create predictor models for chl *a* concentrations in sea ice, we applied Generalized Linear Models (GLM) [*McCullagh and Nelder*, 1989] expressing chlorophyll *a* concentrations as a linear function of combinations of up to five predictor variables (i.e., EOF modes or the modes squared). A GLM includes a link function that describes how the mean depends on the linear predictor and a variance function that describes how the variance depends on the mean [*McCullagh and Nelder*, 1989]. For $N \geq 9$, we selected the first nine EOF modes, and for $N < 9$, we selected the first N EOF modes as predictor variables for the GLM analyses. In addition, each selected EOF mode was squared and included as predictor variables in the GLM analyses.

Following *Taylor et al*. [2013], we assumed a Gaussian error distribution and applied a log-link function for the prediction of chl *a*, i.e., $E(chla_{adj})$. In the GLM model selection cross-validation step, large negative numbers in log space due to the presence of near-zero chl *a* concentrations can result in nondefined error estimates (i.e., infinite RMSE values). To avoid this, all raw chl *a* (*chla*) values were adjusted by a constant value (0.98 mg m^{-2}) so that the minimum chl *a* ($chla_{min} = 0.02$ mg m^{-2}) value was set to 1 mg chl *a* m^{-2}. The adjusted chl *a* values ($chla_{adj}$) were used to fit the models. When the models were fitted with and without the adjustment, differences in BIC were determined to be negligible between adjusted and nonadjusted model fits, and thus did not influence the model selection criteria. In the final model application, the constant (0.98 mg chl *a* m^{-2}) was subtracted before calculating chl *a* estimates of ROV and SUIT profiles.

The GLM models have the form:

$$\ln\left[E\left(chla_{adj}\right)\right] = \alpha + \beta_1 s_1 + \beta_2 s_2^2 + \cdots + \beta_m s_m + \beta_n s_n^2 \tag{8}$$

where $s_{1,2,\ldots,n.m}$ are the EOF modes or the EOF modes squared from S determined from the GLM model selections, α is the intercept and $\beta_{1,2,\ldots,m,n}$ are the regression coefficients.

2.5.2. Normalized Difference Index (NDI)

We constructed a spectral correlation surface matrix between chl *a* concentrations and all possible NDI combinations of two wavelengths within the photosynthetically active radiation (PAR) wavelength range between 400 and 700 nm, as described by *Mundy et al*. [2007]. Correlation surfaces were constructed for each bio-optical model combination (all combinations of bio-optical models are described in section 2.5.4 and visualized in Figure 3). We applied a moving average to the correlation surfaces by taking the mean of a 3 × 3 nm grid centered at each value to ensure maximum chl *a*-NDI correlations were not chosen at the edge of regions of high correlation.

Two maximum chl *a*-NDI correlations were chosen from each correlation surface. The first maximum correlation NDI wavelength combination, NDI_{440}, corresponds to the wider ~440 nm chl *a* absorption peak and has at least one NDI wavelength within the range 400–480 nm. The second maximum correlation NDI wavelength combination, NDI_{670}, corresponds to the narrower ~670 nm chl *a* absorption peak and has at least one NDI wavelength between 655 and 685 nm. We then applied a GLM to the adjusted chl *a* concentrations ($chla_{adj}$: response variable) and NDI (*NDI*: predictor variables) values in the form:

$$\ln\left[E\left(\mathrm{chl}a_{adj}\right)\right] = \alpha + \beta(NDI) \tag{9}$$

where α is the intercept and β the regression coefficient (i.e., slope). *NDI* corresponds to either the maximum chl *a*-NDI correlation NDI_{440} or NDI_{670}. To maintain consistency between statistical approaches, which is important for inter-comparison, we applied a log-link function for all statistical approach models, i.e., $E(chla_{adj})$.

2.5.3. Multi-NDI

In order to take advantage of both chl *a* absorption peaks we incorporated both NDIs (i.e., NDI_{440} and NDI_{670}) into one model. The two maximum NDI correlations for each bio-optical model combination (all combinations described in section 2.5.4 and visualized in Figure 3) were used as predictor variables in GLMs with adjusted chl *a* concentrations ($chla_{adj}$) as the response variable:

$$\ln\left[E\left(chla_{adj}\right)\right] = \alpha + \beta_{440}(NDI_{440}) + \beta_{670}(NDI_{670}) \tag{10}$$

where α is the intercept and $\beta_{440,\ 670}$ are the regression coefficients.

2.5.4. Selection Criteria of Bio-Optical Reference Models

To visualize the selection process from a large number of possible model combinations, we provided a flowchart illustrating the model selection and ranking process following the selection path of one model (Figure 3). Bio-optical models to estimate ice-algal chl *a* were constructed using GLMs based on four different statistical approaches: (1) Empirical Orthogonal Function analysis (EOF); (2) NDI_{440}; (3) NDI_{670}; and (4) multi-NDI (Figure 3a). These statistical approaches were applied to four different spectral measurements: (a) Under-ice Irradiance (E_T); (b) Under-ice Radiance (I_T); (c) Transmittance (T_E); and (d) Transflectance (T_i; Figure 3a). These 16 "statistical approach to spectral measurement" combinations were applied to (1) the full data set (*all*); (2) PS78 cruise (*PS78*); (3) PS80 cruise (*PS80*); (4) high-latitude MYI sites from PS80 (*PS80-MYI*); (5) low-chl *a* (*low*: <2 mg m^{-2}); and (6) high-chl *a* (*high*: >2 mg m^{-2}; Figure 3a).This resulted in 96 "statistical approach to spectral measurement to data subset" combinations, of which 72 were based on the NDI approaches, and 24 were based on the EOF approach.

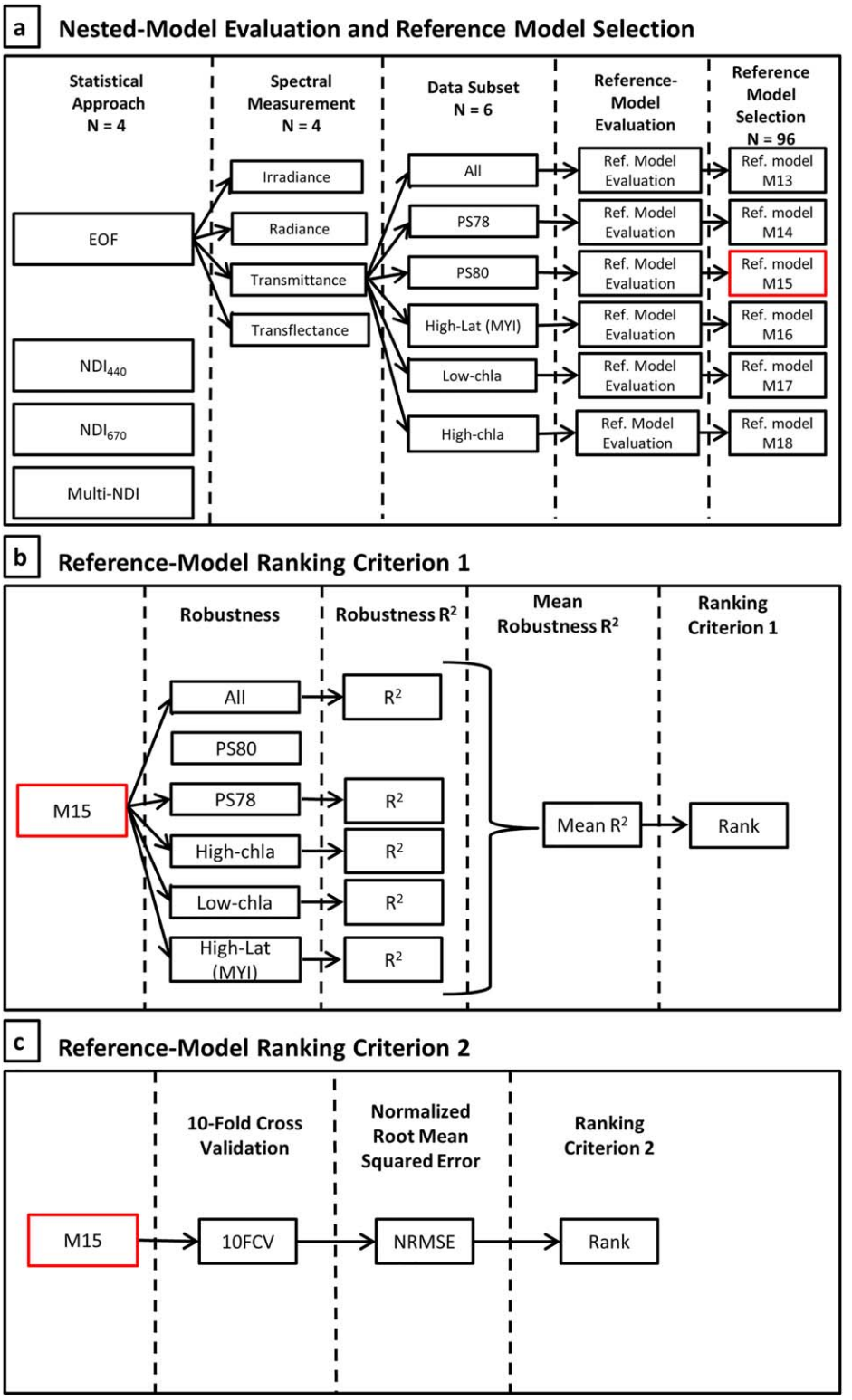

Figure 3. Flowcharts of: (a) reference model evaluation and selection process; (b) reference model ranking criterion 1 based on the mean robustness R2; and (c) reference model ranking criterion 2 based on the normalized root mean squared error (NRMSE). (a) Performed first and results in the selection of one bio-optical model for each of the 96 statistical approach-spectral measurement-data subset combinations. (b and c) Occur independently in parallel and rank the reference models as a means of model inter-comparison. The most reliable models were than ranked based on the average of Figures 3b and 3c. For simplicity, the flowchart only follows the pathway of the top ranked model (M15, referred to in text as EOF-Transmittance).

Within each of these 96 combinations there were multiple potential reference model possibilities of wavelength combinations (NDI) or EOF mode combinations (EOF; Figure 3a). From the many possible NDI-based GLMs, which have various potential combinations of wavelengths, the NDI-wavelength combination with the highest spearman correlation coefficients (Figure 3) was selected as the NDI predictor variable (NDI_{440} or NDI_{670}) or variables (multi-NDI) for fitting the reference model of each 72 corresponding NDI-based approach-spectral measurement-data subset combinations.

For each of the 24 EOF-based spectral measurement-data subset combinations, there were a large number of EOF mode combinations as potential predictor variables in the GLMs. With nine modes, nine squared-modes, and up to five predictor variables, this resulted in over 500,000 different combinations of EOF modes in the GLMs. We used the "*R*" package *glmulti* [*Calcagno and de Mazancourt*, 2010], to select the "best" 100 GLMs from all possible unique combinations of predictor variables based on a predefined model evaluation criterion. The *glmulti* package has built-in functions using Akaike Information Criterion (AIC) or Bayesian Information Criterion (BIC) for model selection [*Calcagno and de Mazancourt*, 2010]. Here we selected BIC over AIC, because the AIC accounts for only the sample size, whereas the BIC accounts for both the number of predictor variables included in the GLM and the number of samples used to fit the GLM [*Schwarz*, 1978]. Hence, a smaller number of predictor variables will result in a better model BIC than a larger number of predictor variables, and a larger sample size will result in a better model BIC than a smaller sample size. Out of these 100 "best" potential models (GLMs) for each of the 24 EOF-based spectral measurement-data subset combinations, we selected one reference model, which had the lowest BIC and in which all coefficients were significant ($p \leq 0.05$) (Figure 3a).

2.5.5. Comparing Reference Models and Identifying Predictive Models

The previous selection process identified the most reliable reference model for each of the 96 statistical approach to spectral measurement to data subset combinations (Figure 3a). In order to assess the reliability of these reference models to predict ice-algal chl *a* concentrations in larger spectral data sets, such as from under-ice profiling platforms (e.g., ROV and SUIT), we ranked the 96 reference models based on two criteria (Figures 3b and 3c). Based on the average of both rankings, we selected the top five models as the most reliable set of potential "predictive models" for further comparison.

For the first ranking criterion (Figure 3b), we assessed model robustness, applying an adapted procedure used by *Melbourne-Thomas et al*. [2015]. Each of the 96 reference models was applied to the 5 data subsets not used to fit the respective reference model. For example, the EOF-Transmittance model fitted to the PS80 data subset was applied to the other five data subsets (All, PS78, High-chla, low-chla, and High-lat) but not applied to the PS80 subset because the model was fitted to this data (Figure 3b). We then calculated the predicted chl *a* versus observed chl *a* coefficient of determination (R^2) for each reference model applied to each of the five data subsets, which we refer to as the robustness R^2. We calculated the mean of the robustness R^2 values for each data subset. The mean robustness R^2 provides an estimate of how well the models perform when applied to "new" spectral data (e.g., larger-scale ROV or SUIT spectra) and may also identify variability in how the models fit different cruises (PS80 versus PS78) or chl *a* concentrations (high versus low). The mean robustness R^2 values were ranked from highest to lowest and used as the first criterion for selecting the top five potential predictive models. One limitation of this ranking criterion is that subsets were preselected by nonrandom factors, which may introduce bias. This is why we included an additional ranking criterion, which uses random data subsets to evaluate predictive power of the models.

Models are optimized for the data they are fitted to (i.e., training data); therefore the error of the model applied to new data (true prediction error) is usually higher than when the model is applied to the training data (training error). It is common to use training error estimates (e.g., trained model residuals) for the selection of models or to report confidence intervals for predicted data [e.g., *Taylor et al*., 2013]. This can result in the selection of inferior models or an inaccurate estimate of the true prediction error. Taking these considerations into account, we implemented a second model ranking criterion in order to select the predictive models. The second ranking criterion is based on 10-Fold Cross-Validation (10FCV) to estimate the true prediction error of each model. K-fold cross validation is a commonly used method to assess the performance of predictive models by providing accurate estimates of the true prediction error [*Mahmood and Khan*, 2009]. In 10FCV, the data are first subset into 10-folds (i.e., data subsets). Model fitting and error estimation are repeated 10 times. Each time a different set of ninefolds are combined to train/fit the model. Each model is then applied to the 10th fold of "new" spectral data (i.e., holdout data). The root mean square error

(RMSE) is calculated for the "new" predicted chl *a* data, which provides an estimate of the true prediction error. The 10 error estimates (RMSE) are averaged to provide a more robust RMSE estimate for each 10FCV run. Since the data are subset randomly, the 10FCV process is repeated 100 times to ensure more representative subsampling of the data and a more representative estimate of the true prediction error (RMSE). The 10FCV procedure results in one estimate of the true prediction error for each model, which we term the cross-validation RMSE ($RMSE_{CV}$). The $RMSE_{CV}$ is used as an indicator for the quality of the model, with lower $RMSE_{CV}$ values corresponding to models with a higher predictive performance. The $RMSE_{CV}$ is also used to provide model uncertainty estimates when models are applied to new spectral data (e.g., ROV and SUIT spectral radiation profiles).

In order to compare between models with different sample sizes and range of values we normalized the $RMSE_{CV}$ by the range (minimum and maximum) of observed chl *a* values ($chla_{obs,min}$ and $chla_{obs,max}$) used to train the model. $NRMSE_{CV}$ was calculated as:

$$NRMSE_{CV} = \frac{RMSE_{CV}}{chla_{obs,max} - chla_{obs,min}} \tag{11}$$

$NRMSE_{CV}$ values were ranked from lowest to highest and used as the second criterion for selecting the top five potential predictive models. The rankings of the mean robustness R^2 (first criterion) and $NRMSE_{CV}$ (second criterion) were then averaged and ranked to arrive at the top five ranked potential predictive models. Robustness of statistical assumptions in these five predictive GLMs were visually assessed based on validation plots. Because we have limited data points in the high-chl *a* range, particular attention was given to the leverage of each point and identification of potential model fit outliers. Following procedures described in *Aguinis et al*. [2013], we first identified potential model fit outliers using a Cook's *D* cutoff value equal to the *F* statistic (~0.92). Second, we fitted the models with removal of the identified potential outliers and assessed the change in model fit statistics: R^2, BIC, and model significance [*Aguinis et al*., 2013]. Model fit outliers were only reported if statistically significant changes in model fit were observed. Model significance was assessed with an analysis of variance (ANOVA) using the *F* test.

Further quality assessments were conducted on the top five predictive models in order to ensure these models were acceptable for application to larger scale spectral data. This included: (i) investigating any potential relationships between environmental properties and chl *a*, which may influence model performance; (ii) evaluating the biases of the model, and the model applied to high-chl and low-chl *a*, e.g., if the model over-estimates (positive bias) or under-estimates (negative bias) the predicted data; (iii) applying the potential predictive models (excluding any models identified as unreliable from the previous two steps) to larger-scale spectral profiles and comparing general performance between predictive models for all profiles; and *iv)* assess predictive performance of each potential predictive model along a short 85 m ROV transect and compare to ice core chl *a* observations along the same transect.

2.5.6. Predicting Ice-Algal chl *a*

We applied the selected most reliable predictive models to independent spectral measurements from two SUIT stations and two ROV stations conducted during the *PS80* cruise. These included high-latitude stations PS80/358 (SUIT) and PS80/360 (ROV ice station), and lower-latitude stations PS80/285 (SUIT) and PS80/323 (ROV ice station; Figure 1). These stations were selected in order to compare the predictive models applied to independent data from different regions and different environmental conditions.

The application of NDI models to independent spectral measurements required first to calculate the $NDI_{\lambda 1:\lambda 2}$ using the wavelength combinations (e.g., $\lambda 1$ and $\lambda 2$) from NDI-based predictive models. The *NDI* values were then incorporated into equation (9) (NDI model) or equation (10) (multi-NDI model) along with α and β values predetermined by the predictive models to derive the corresponding chl *a* concentrations.

Predictions of chl *a* concentrations on new spectral data using the EOF method were conducted as described in *Taylor et al*. [2013]. The independent spectral measurements were first standardized, as described previously. The independent standardized spectral data Y, a $J \times M$ matrix with *J* the number of independent spectral measurements and *M* the number of wavelengths, was then projected onto the EOF expansion coefficients Z in the form:

$$\mathrm{F} = \left(Z^{-1}\mathrm{Y}\right)^{T} \tag{12}$$

where F, the EOFs, is a $J \times J$ matrix providing the loadings by mode (*J*) for each sample (*J*), as with S. Predicted ice-algal chl *a* values were calculated using the EOF-based predictive models' GLM formula and the new EOFs, F, in the form:

$$\ln\left[E\left(chla_{\text{pred}}\right)\right]=\alpha+\beta_1 f_1+\beta_2 f_2^2+\cdots+\beta_n f_n+\beta_m f_m^2 \quad (13)$$

where $f_{1,2,\ldots,n,m}$ are the EOF modes or modes squared from F, which correspond to the selected modes from S (e.g., $s_{1,2,\ldots,n,m}$) used as response variables in equation (8), α is the intercept and $\beta_{1,2,\ldots,n,m}$ the regression coefficients from equation (8).

The $chla_{pred}$ values were readjusted by subtracting 0.98 mg chl *a* m^{-2} to account for the premodel adjustment of the chl *a* values. Due to the range of observed chl *a* values ($\sim$0–12 mg chl *a* m^{-2}), the predicted chl *a* were limited to a range of 0–20 mg chl *a* m^{-2} by excluding all other values. We set these limits because predicting values significantly outside the range of data they were trained on only increases uncertainty in the predicted data. Ice algae biomass values of up to 22 mg chl *a* m^{-2} [*Melnikov* 1997] and 14 mg chl *a* m^{-2} [*Gosselin et al*. 1997] have been reported within the same study region and season in the Arctic Ocean. Therefore, setting an upper limit to 20 mg chl *a* m^{-2} was deemed acceptable in order to limit two different potential sources of error. First, it limits potential negative biases (i.e., underestimation) of the overall observations by not accounting for high biomass regions if we had imposed too strict of an upper limit. Second, it limits the potentially higher prediction uncertainty for high biomass values outside the range of values the model was trained on.

3. Results and Discussion

3.1. Environmental Properties

Both expeditions covered large geographical regions and were conducted during the transition from late-melt to the onset of freeze-up, and thus encountered a large range of sea ice conditions. Sea ice conditions during all ice stations were summarized in Table 1. Information about individual ice core samples was summarized in supporting information Table S1. During PS78, sea ice stations were conducted from the Eurasian shelf edge to the Canadian Basin and back again. This sampling effort captured the transition from ice-edge through first-year ice and into the multiyear pack-ice. During ice stations PS78/198, PS78/203, and PS78/212 the surrounding sea ice was in an advanced state of melt with no snow cover and open melt ponds. Freeze-up conditions were first observed on 22 August, characterized by the presence of a light snow cover and surface freezing of melt ponds, and continued during the remaining ice stations PS78/227, PS78/238, and PS78/245.

During PS80, the first two ice stations, PS80/224 and PS80/237, were situated in densely packed first-year ice. Ice stations PS80/255, PS80/277, and PS80/323 were conducted in a region dominated by rotten sea ice with modal ice thicknesses $<$1.0 m. A thin snow cover was first observed at station PS80/323 and was present at the remaining stations, but did not exceed 0.1 m. Station PS80/335 was situated in an area of mixed FYI and MYI with no obvious signs of advanced melt or freeze-up, indicating it was in transition from melt to freeze-up conditions. Freeze-up conditions were first observed at station PS80/349, characterized by ice forming on the surface of melt ponds, and continued for the remaining stations. Ice stations PS80/349 and PS80/360 were conducted within the heavy pack-ice consisting of predominantly MYI with thicknesses $>$1.5 m. The first ice station PS80/224 was revisited as station PS80/384 and was then characterized by fall freeze-up and an ice thickness of $\sim$1 m. The range of modal ice thicknesses for the FYI stations (0.8–1.3 m) were consistent with previous large-scale airborne and floe-scale ground-based electromagnetic ice thickness surveys conducted for the same region and season [*Haas and Eicken*, 2001; *Haas et al*., 1997; *Rabenstein et al*., 2010]. The two MYI sites with modal thicknesses of 1.6 and 1.8 m were characteristic of MYI and consistent with modal ice thickness values for second-year sea ice from the same region and season [*Haas and Eicken*, 2001]. Further details about the environmental properties encountered during these two cruises are presented in other studies [e.g., *Boetius et al*., 2013; *Fernández-Méndez et al*., 2014; *Katlein et al*., 2014a; *Nicolaus and Katlein*, 2013].

All observations were made in late summer at the end of the productive season. Thus, algal biomass was relatively low during both cruises. Of the 14 bio-optical cores collected during PS78, none of the samples exceeded 1.0 mg chl *a* m^{-2} (Table 1). Of the 59 bio-optical cores collected during PS80, however, samples exceeded 1.0 mg chl *a* m^{-2} at 6 out of the 10 ice stations (PS80/237, PS80/255, PS80/335, PS80/349, PS80/360, and PS80/384). Maximum chl *a* concentrations were observed at MYI station PS80/360, with three of the four ice cores ranging between 6.4 and 11.8 mg chl *a* m^{-2} (Table 1). Also noteworthy was MYI station

PS80/349, which had the next highest chl *a* concentrations with two cores at 3.5 and 5.6 mg chl *a* m^{-2} (Table 1). The high biomass we observed at the high latitude MYI stations is consistent with previous studies from high latitude regions of the central Arctic Ocean with bottom-ice algae concentrations in the range of 3–14 mg chl *a* m^{-2} [*Gosselin et al*., 1997] and up to 22 mg chl *a* m^{-2} [*Melnikov*, 1997]. *Gosselin et al*. [1997] also observed a shift from low to high bottom-ice biomass with a shift from low to high latitude, which is consistent with our chl *a* biomass values.

3.2. Spectral Measurements

Daily mean incident solar radiation (E_S) generally decreased during both cruises and also decreased with latitude, which was evident by the negative correlations of E_S with day of the year and latitude (Table 2). Incident solar radiation (PAR) was typically over 35 W m^{-2} except at stations PS78/227, PS80/349, PS80/360, and PS80/384, which fell below 20 W m^{-2} (Table 1). These values were expected for the sampling season and regions [*Gosselin et al*., 1997]. ROV-derived spectral properties of the sea ice were presented and discussed in *Nicolaus and Katlein* [2013] and *Nicolaus et al*. [2012] for PS78, and in *Katlein et al*. [2014b] for PS80. Of the 73 bio-optical core locations, under-ice irradiance (E_T) and transmittance (T_E) spectra from 49 core locations, and under-ice radiance (I_T) and transflectance (T_I) spectra from 50 core locations were deemed of high quality and used for the development of bio-optical models (supporting information Table S1).

During summer, snow effects can generally be neglected due to a lack of snow [*Nicolaus et al*., 2012], which is applicable to both cruises as the presence of snow never exceeded 0.1 m. Strong negative correlations were observed for ice thickness with T_E and T_I (Table 2). The strong correlation of ice thickness with T_E and T_I is a result of the large range of ice thicknesses sampled (e.g., 0.05–3.53 m) in combination with the strong influence of ice on light transmittance. The observed highly variable ice conditions had a large influence on light transmission, which showed horizontal variability of one to two orders of magnitude on the same ice floe for both FYI and MYI [*Nicolaus et al*., 2012]. The observed horizontal variability on the same ice floe is the result of the influence of melt ponds on light transmittance. The length scale of melt-pond variability was closely related to the length scale of light transmittance [*Katlein et al*., 2015; *Perovich et al*., 1998; *Petrich et al*., 2012] due to the higher transmittance of melt ponds [*Nicolaus et al*., 2012]. Overall, FYI showed higher transmittance than MYI during PS78 [*Nicolaus et al*., 2012], which was also the case for PS80. The observed difference between MYI and FYI is mainly influenced by melt-pond coverage since relatively similar transmittance values were observed during PS78 when compared between white (not ponded) MYI (0.01) and white FYI (0.04), and between ponded MYI (0.15) and ponded FYI (0.22) [*Nicolaus et al*., 2012]. This pattern is consistent with literature values of transmittance for FYI and MYI in other regions of the Arctic Ocean during summer [*Light et al*., 2008; *Perovich et al*., 1998]. Furthermore, FYI has a larger areal coverage of melt ponds compared to MYI, which causes FYI to have nearly a threefold greater total (PAR) areally averaged transmittance (0.11) compared to MYI (0.04) [*Nicolaus et al*., 2012].

Critical minimum under-ice irradiance, E_T, levels for algal growth have been reported between 0.4 and 2.0 W m^{-2} (2–9 μmol photons m^{-2} s^{-1}) [e.g., *Gosselin et al*., 1986; *Horner and Schrader*, 1982; *Lange et al*., 2015]. Stations PS80/360 and PS80/384 had mean E_T values below this critical range (<0.4 W m^{-2}); stations PS78/

Table 2. Pearson Correlation Coefficient Matrix for all Combinations of Bio-Optical Core Location Bio-Environmental Variables

	Snow	Scat.	Ice	Day	Lat.	E_S	E_T	T_E	I_T	T_I
chla	0.05	−0.07	0.08	0.27*	**0.47***	−0.28*	−0.22	−0.17	−0.22	−0.15
Snow		−0.20	0.08	0.37*	0.10	0.05	−0.30*	−0.29*	−0.31*	−0.33*
Scat.			0.23	**−0.40***	−0.18	0.14	−0.16	−0.22	−0.08	−0.14
Ice				−0.26*	0.03	0.11	−0.37*	**−0.47***	−0.33*	**−0.51***
Day					**0.46***	**−0.56***	−0.20	0.09	−0.25	0.13
Lat.						**−0.68***	−0.12	0.19	−0.32*	0.03
E_S							0.14	−0.21	0.29*	−0.18
E_T								**0.82***	**0.94***	**0.78***
T_E									**0.65***	**0.97***
I_T										**0.73***

*Indicates significant correlation at $p \leq 0.05$.

Bold values indicate strong correlations ≥0.4.

Chla is the chlorophyll *a* concentration; ice is the sea ice thickness; day is the day of the year starting from January 1. Lat. is latitude; Scatt. is the scattering surface layer depth; E_S is incident solar radiation; E_T is under-ice irradiance; T_E is spectral transmittance; I_T is under-ice radiance; T_I is spectral transflectance.

227, PS78/238, PS78/245, and PS80/349 had mean E_T values within this critical range (0.4–2.0 W m^{-2}); and all other stations were above this critical range (Table 1). Even though the high-latitude stations PS80/360 and PS80/349 had mean E_T values below or within the critical range these stations still had the highest mean ice core chl *a* concentrations compared to the other stations. Loss of algal biomass in summer is primarily the result of losses due to ice melt [e.g., *Grossi et al*., 1987], and substantial loss of ice-algal biomass had likely occurred prior to our sampling in 2012 [*Boetius et al*., 2013]. The higher latitude and dominance of thicker MYI at stations PS80/360 and PS80/349 probably resulted in lower melt rates, due to less internal energy absorption by MYI compared to FYI [*Nicolaus et al*., 2012], and subsequently less algal biomass loss due to melt before our sampling.

3.3. Model Performance

3.3.1. Comparison of Statistical Approaches

The two highest-ranking predictive models were based on an EOF approach, and had considerably higher R^2 values ($\geq$0.9) and lower RMSE values ($<$0.8) than all other predictive models (Table 3). The two NDI-based predictive models in our selection were based on the "high-chl *a*" data subset ($N = 15$), using radiance data (rank 3) and transmittance data (tied for rank 4), respectively. Only the EOF models ranked first and fourth, however, combined large data subsets ($N = 38$ and $N = 50$, respectively), which suggests these models are more reliable than the best ranked NDI models with smaller samples sizes. The most reliable EOF models also incorporated spectral measurements that take into consideration the incoming solar radiation, indicating a wide applicability under varying incoming light conditions (Table 3). Furthermore, the inclusion of larger data sets by these EOF models indicates that these models can account for the large range of environmental conditions (e.g., sea ice thickness, scattering layer depth, and melt ponds) experienced during the cruises.

Based on the model biases, there appear to be no obvious trends between statistical approaches of the five most reliable predictive models, with all values near zero (Table 3). However, the biases of the models applied to the high-chl *a* and low-chl *a* data demonstrate that the NDI-based approaches underestimate the high-chl *a* data while overestimating the low-chl *a* data. The EOF-based approaches demonstrated low model biases and low biases when applied to both high-chl *a* and low-chl *a* data. The cause of the higher biases for the NDI-based approaches was likely the result of the large range of environmental conditions experienced during the cruise. This had a large influence on the variability of the spectral radiation measurements, which was not sufficiently accounted for in the NDI models.

A complete list summarizing all 96 reference models for each combination of spectral measurement with a statistical approach and a data subset was provided in supporting information Table S2. Based on the

Table 3. Summary of the Top Five Predictive Models

Model ID		EOF-Transmittance	EOF-Radiance	NDI_{670}-Irradiance	EOF-Transflectance	NDI_{670}-Transmittance
N (sample size)		38	15	15	50	15
Equation: $\ln[E(chl\ a_{adj})] =$		$0.7 - 3.0s_2 + 1.1s_4 + 2.4s_6 - 6.5s_7^2 + 3.9s_9^2$	$2.0 + 2.7s_4 - 1.7s_5 - 1.0s_6 - 2.3s_2^2 - 10.0s_8^2$	$2.2 + 10.8NDI_{669:683}$	$0.3 + 1.5s_2 - 1.7s_4 + 2.0s_7 + 3.2s_9 + 8.6s_9^2$	$1.2 - 11.1NDI_{678:684}$
Model	R^2	0.90	0.95	0.73	0.74	0.70
	RMSE	0.77	0.66	1.58	1.12	1.65
	bias	−0.02	−0.08	0.02	−0.12	0.06
Bias of model applied to subset:	High-chl*a*	−0.01	−0.08	0.02	−0.01	0.06
	Low-chl*a*	0.00	0.00	2.09	0.00	1.96
R^2 of model applied to subset:	All	0.88	0.56	0.54	NA	0.63
	PS78	−0.11	NA	−0.08	NA	0.01
	PS80	NA	0.55	0.60	0.74	0.64
	MYI	0.94	0.55	0.68	0.76	0.62
	Low-chl*a*	−0.01	−0.02	0.07	0.00	0.06
	high-chl*a*	0.93	NA	NA	0.82	NA
	mean[a]	0.53	0.41	0.36	0.58	0.39
Cross validation	RMSE	1.81	1.81	1.89	2.46	2.01
	NRMSE[b]	0.15	0.17	0.18	0.21	0.19
Ranking	R^2 mean[a]	4	9	13.5	2	11
	NRMSE[b]	6	7	8	23	14
	Mean	1	2	3	4.5	4.5

[a,b]Depict the matching model statistic and corresponding ranking criterion variable.

model R^2 values, the EOF-based models performed generally better than the three NDI-based approaches (supporting information Table S2). Among the NDI-based approaches, multi-NDI and NDI_{670} performed best. The good performance of the multi-NDI approach was probably driven by good relationships in the NDI_{670} values because overall the NDI_{440} models demonstrated the lowest R^2 values.

Similar studies have provided no model error estimate [e.g., *Melbourne-Thomas et al*., 2015] or provided the model RMSE [e.g., *Campbell et al*., 2014; *Taylor et al*., 2013] as a measure of model uncertainty, which is always an underestimate of the true prediction error. The true prediction error estimate is particularly important to assess the uncertainty of predictions made using new (spectral) data. Here we provided an assessment of the true prediction error for the models using $RMSE_{CV}$ values (Table 3), which are often over double the model RMSE values (Table 3). For our predictive models, these values appear to be in an acceptable range considering the variability of environmental conditions. For comparison, all predictive models true prediction error estimates, $RMSE_{CV}$ (Table 3), were lower than the model RMSE provided by *Campbell et al*. [2014].

All five selected predictive models demonstrated high variability in predicting low-chl *a* values of the low-chl *a* subset and the *PS78* data subset (i.e., $<$2 mg msupporting information^2; Table 3). This is expected, since with low-chl *a* concentrations there is less absorption of light by algal biomass, which enhances the relative influence of other environmental properties on the transmitted spectra, such as ice thickness, scattering layer and melt ponds. The two selected predictive models based on NDI_{670} had relatively large positive biases when applied to low-chl *a* (Table 3), suggesting that the NDI_{670} models applied to independent data may also result in overestimation of low-chl *a* regions. This is not surprising since these two NDI-based predictive models were fitted to high-chl *a* data. Even though the EOF models also had large errors associated with predicting the variability of low-chl *a*, these models had practically no directional bias when applied to low-chl *a* and high-chl *a* (Table 3), suggesting that these EOF models can correctly differentiate between low, medium, and high-chl *a* concentrations, and are less likely to result in over-estimations or under-estimations when applied to independent spectral data.

An overall better performance of models using an EOF-based approach can be attributed to the fact that the EOF method accounted for a larger range of spectral variability by including multiple regions of the spectra, which were represented by the different EOF modes. Wavelength-dependent changes in the shape of the radiance spectra due to, e.g., ice thickness or melt ponds, were captured by the dominant signal of spectral variability, mode 1. The fact that mode 1 was not included in the most reliable model and because the modes are orthogonal, implies that the EOF approach accounts for this wavelength-dependent variability within mode 1 (i.e., it removes the influence from other modes). Therefore, other modes can show more of the spectral variability caused by chl *a* absorption. In ocean color remote sensing, increasingly complex algorithms have been developed to include more spectral bands in order to account for the many variables that influence ocean optics other than phytoplankton chl *a* [e.g., *Craig et al*., 2012]. In the ocean, this is mostly CDOM or particles, but for sea ice, the snow and ice matrix generally have a much larger influence on light penetration compared to any single variable in the ocean. The variability of under-ice and incoming spectra was particularly important during our study due to the large range of environmental properties experienced in terms of latitude, ice thickness, state of melt, and melt-pond coverage. In comparison, previous studies were performed in more uniform ice properties over a smaller latitudinal range [e.g., *Campbell et al*., 2014, 2015; *Melbourne-Thomas et al*., 2015; *Mundy et al*., 2007].

The modes of oscillation (Figure 4) show the signatures of change within the spectral measurements due to different variables that influence the transmission of light through sea ice. Mode 1 alone explained most of the spectral variability ($\sim$95%), but was not selected in any reference model. This is not surprising, since the shape of the mode of oscillation closely resembles that of the spectral extinction coefficient curves for snow and ice [*Grenfell and Maykut*, 1977]. Furthermore, mode 1 had a significant medium-to-strong correlation with the presence of melt ponds, indicating that melt ponds had a large influence on spectral variability. This is expected since melt ponds are known to transmit more light [e.g., *Katlein et al*., 2015; *Light et al*., 2008; *Nicolaus et al*., 2012].

For each of the modes included in the EOF-transmittance model (modes 2, 4, 6, 7, and 9) there was at least one local maximum or minimum corresponding to one of the maximum chl *a* absorption regions (Figure 4). Accordingly, four out of five modes, for both EOF-based predictive models, have medium to strong

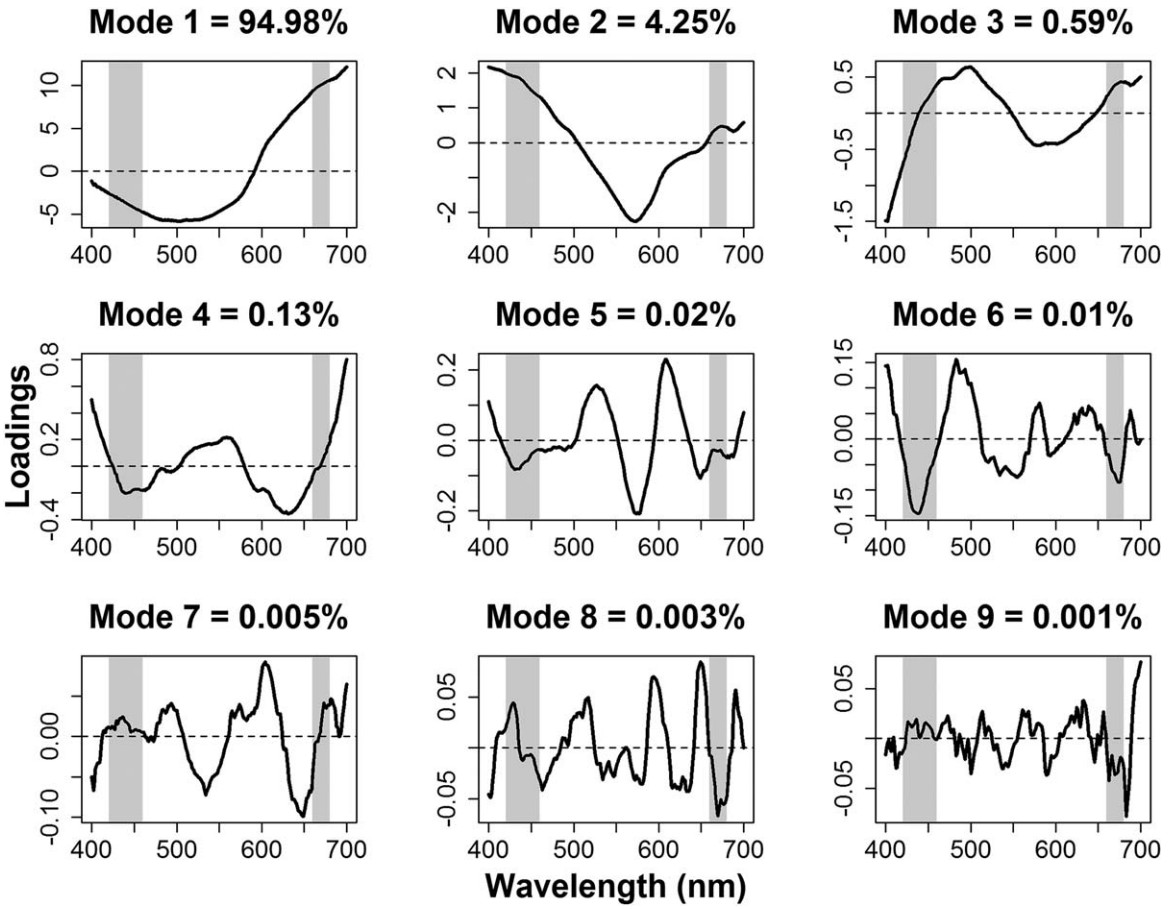

Figure 4. EOF modes represented as modes of oscillation in the entire standardized spectral Transmittance data set. The modes of oscillation were calculated by projecting the spectral matrix (X) onto the EOF matrix (S), showing the loadings for each wavelength by mode. Included is the proportion of variance explained by each corresponding mode. Gray shaded areas represent the maximum chl a absorption regions centered at 440 and 670 nm.

significant correlations with chl *a*, and two of the five modes for the EOF-Transmittance model (s_6 and s_9^2) and one of five modes used in the EOF-Transflectance model (s_7) have strong significant correlations with only chl *a* (Table 4). The modes that have strong correlations with only chl *a* also are associated with high changes in BIC when the term is removed from the model.

The proportion of variance explained by the modes used in the selected most reliable EOF-based predictive models was relatively low compared to those found in other studies [e.g., *Craig et al.*, 2012; *Melbourne-Thomas et al.*, 2015]. *Taylor et al.* [2013] included modes 5–9 in their analyses and showed that even subordinate modes which explained smaller proportions of the spectral variance still had an important influence on the models based on change in the Akaike Information Criterion (AIC). Their study related spectral radiance to phycoerythrin concentrations, which is an accessory pigment and therefore has a smaller influence on light absorption compared to chl *a*. This could explain why the subordinate modes were important in the model, since they captured the smaller variations caused by the spectrally less influential phycoerythrin pigment [*Taylor et al.*, 2013]. Similarly, during our study, ice-algal chl *a* concentrations had a smaller influence on spectral light transmission relative to, e.g., ice thickness, melt ponds, incoming light and solar inclination. Because the physical properties of the snow and ice matrix dominate the influence of light transmission, the variability of chl *a* concentrations in sea ice appears to be best represented by subordinate modes explaining a smaller part of the EOF variability compared to approaches estimating chl *a* concentrations in water.

3.3.2. Comparison of Spectral Measurements

Significant correlations of ice core chl *a* with latitude and ice core chl *a* with solar radiation (Table 3) suggest that care is needed when interpreting models that do not account for the variability of incoming solar

Table 4. Correlation Matrix Between EOF Modes (s_1–s_9, s_1^2–s_9^2) and Bio-Environmental Properties for the Three Most Reliable EOF models[a]

Model	Variable	s_1	s_2	s_3	s_4	s_5	s_6	s_7	s_8	s_9	s_1^2	s_2^2	s_3^2	s_4^2	s_5^2	s_6^2	s_7^2	s_8^2	s_9^2
EOF-Transmittance	Model Terms		s_2		s_4		s_6										s_7^2		s_9^2
	Chl *a*	0.28	−0.35*	−0.08	0.33*	−0.04	0.49*	0.18	−0.04	−0.36*	−0.28	0.29	−0.04	0.08	0.04	0.63*	0.21	0.06	0.59*
	Melt pond	0.38*	−0.32*	−0.40*	−0.10	−0.25	−0.15	−0.20	0.14	−0.12	−0.38*	0.37*	0.36*	0.18	−0.03	0.12	0.36*	0.32	−0.10
	snow	−0.07	−0.13	0.49*	0.08	0.55*	−0.10	0.18	0.11	−0.16	0.06	−0.08	0.28	0.03	0.37*	−0.07	0.02	−0.14	0.06
	Scatt.	−0.15	0.33*	−0.13	0.19	0.03	0.10	−0.26	−0.37*	0.25	0.16	−0.16	−0.16	−0.07	−0.26	−0.25	−0.22	−0.10	−0.04
	ice	−0.15	0.43*	−0.10	0.53*	0.40*	−0.06	−0.06	−0.18	0.03	0.15	−0.16	−0.01	−0.15	−0.13	−0.15	−0.22	−0.17	0.17
EOF-Transflectance	Model Terms		s_2		s_4			s_7		s_9									s_9^2
	Chl *a*	0.25	0.31*	0.00	−0.32*	−0.10	0.01	0.36*	0.27	0.34*	−0.24	0.24	−0.07	0.16	0.18	0.20	0.41*	0.03	0.13
	Melt pond	0.39*	0.28*	0.42*	−0.10	−0.27	0.17	−0.21	−0.03	−0.04	−0.40*	0.40*	−0.02	0.16	−0.06	0.45*	−0.04	0.02	0.03
	snow	−0.07	0.19	−0.53*	0.05	0.43*	−0.15	0.18	0.03	0.32*	0.06	−0.09	0.45*	0.00	0.33*	−0.12	0.17	−0.16	−0.04
	Scatt.	−0.04	−0.29*	0.04	−0.14	−0.07	−0.06	−0.01	−0.32*	−0.28	0.03	−0.02	−0.13	−0.06	−0.11	−0.11	−0.17	0.30*	0.03
	ice	−0.16	−0.52*	−0.24	−0.47*	0.25	−0.05	−0.18	0.07	−0.13	0.16	−0.17	0.24	−0.11	−0.10	−0.26	0.15	0.02	−0.01
EOF-Radiance	Model Terms				s_4	s_5	s_6					s_2^2						s_8^2	
	Chl *a*	0.19	0.15	−0.04	0.63*	−0.23	0.05	−0.25	0.18	−0.38	−0.19	0.20	−0.14	0.28	0.03	−0.23	0.30	−0.19	0.05
	Melt pond	0.55*	−0.53*	0.31	0.39	−0.57*	−0.10	−0.03	−0.26	0.10	−0.53*	0.52*	0.32	0.15	0.56*	0.25	−0.34	0.28	−0.21
	snow	0.17	−0.32	−0.61*	0.10	0.51	−0.30	−0.06	0.11	−0.14	−0.21	0.21	0.27	−0.42	0.04	0.00	0.46	−0.12	−0.23
	Scatt.	−0.40	0.14	0.46	−0.70*	0.16	0.06	−0.17	−0.16	0.20	0.42	−0.42	−0.26	0.33	−0.28	−0.37	−0.50	−0.23	0.44
	Ice	−0.13	0.24	0.00	−0.10	0.89*	−0.08	0.10	0.02	0.11	0.11	−0.10	−0.21	−0.15	−0.46	−0.15	−0.03	−0.07	0.00

Refers to significant correlations at $p \leq 0.05$; Scatt. is the depth of the surface scattering layer. Snow is snow depth; ice is the ice core length; s_1 *to* s_9 are EOF modes 1 to 9; s_1^2 to s_9^2 are EOF modes 1–9 squared.

[a]Model terms show only the modes used as terms in the corresponding model.

radiation (i.e., under-ice irradiance and radiance). Of the five selected predictive models, the lowest-ranking NDI_{670} model uses under-ice irradiance for the high-chl *a* data subset. In this data subset there was a significant negative correlation between chl *a* and incoming solar radiation ($r = -0.58$, $n = 15$, $p = 0.02$), and a trend between chl *a* and under-ice irradiance ($r = -0.46$, $n = 15$, $p = 0.08$). No correlation was observed between chl *a* and integrated transmittance for the high-chl *a* data subset. The fact that these variables already showed a significant correlation implies that building a model with these two variables may influence the model in an unknown way. For example, the observed correlation between chl *a* biomass and the strength of the incoming light field may produce artificially high predictive performance of these models, which is not due to the chl *a* absorption of the light. In contrast, the fact that transmittance was not significantly correlated with chl *a* biomass provides more reliability in models built from these spectral data. Because we cannot be certain to what extent the performance of the irradiance-based and radiance-based models were influenced by variations within the incoming solar irradiance, we excluded the two selected predictive models using under-ice radiance and irradiance data (e.g., EOF-radiance and NDI_{670}-irradiance) from further analyses.

Previous studies presented reliable models for estimating ice-algal chl *a* concentrations using under-ice irradiance, which do not account for variations of incoming solar radiation. These studies covered small local study regions during early spring [*Mundy et al*., 2007] and spring-summer transition [*Campbell et al*., 2014, 2015], and had a comparably lower latitudinal range during austral spring [*Melbourne-Thomas et al*., 2015], and therefore had less variability in the magnitude of the incoming light field. These studies were also conducted during a time when snow had a dominant influence on light transmittance. This together with the generally better performance of transmittance and transflectance models suggests that incoming solar radiation should always be measured and accounted for in bio-optical predictive models extending over a large spatial and/or temporal range. The additional time and logistical requirements incurred by operating an additional sensor is minimal making it all the more realistic to incorporate this important methodological advancement in future field programs.

3.4. Bio-Optical Predictive Model Up-Scaling

The aim of model development and selection was to derive a predictive model that is best at estimating ice-algal chl *a* concentrations from independent spectral data over large spatial scales collected by an ROV and a SUIT. The EOF-Transmittance (PS80 data subset, $N = 38$) model was chosen as the most reliable predictive model based on the ranking of the mean robustness R^2 and the NRMSE (Table 3). We excluded the EOF-radiance predictive model (ranked second) and NDI_{670}-irradiance predictive model (ranked thrid; Table 3) due to correlations of chl *a* with incoming light and under-ice irradiance, which left the EOF-

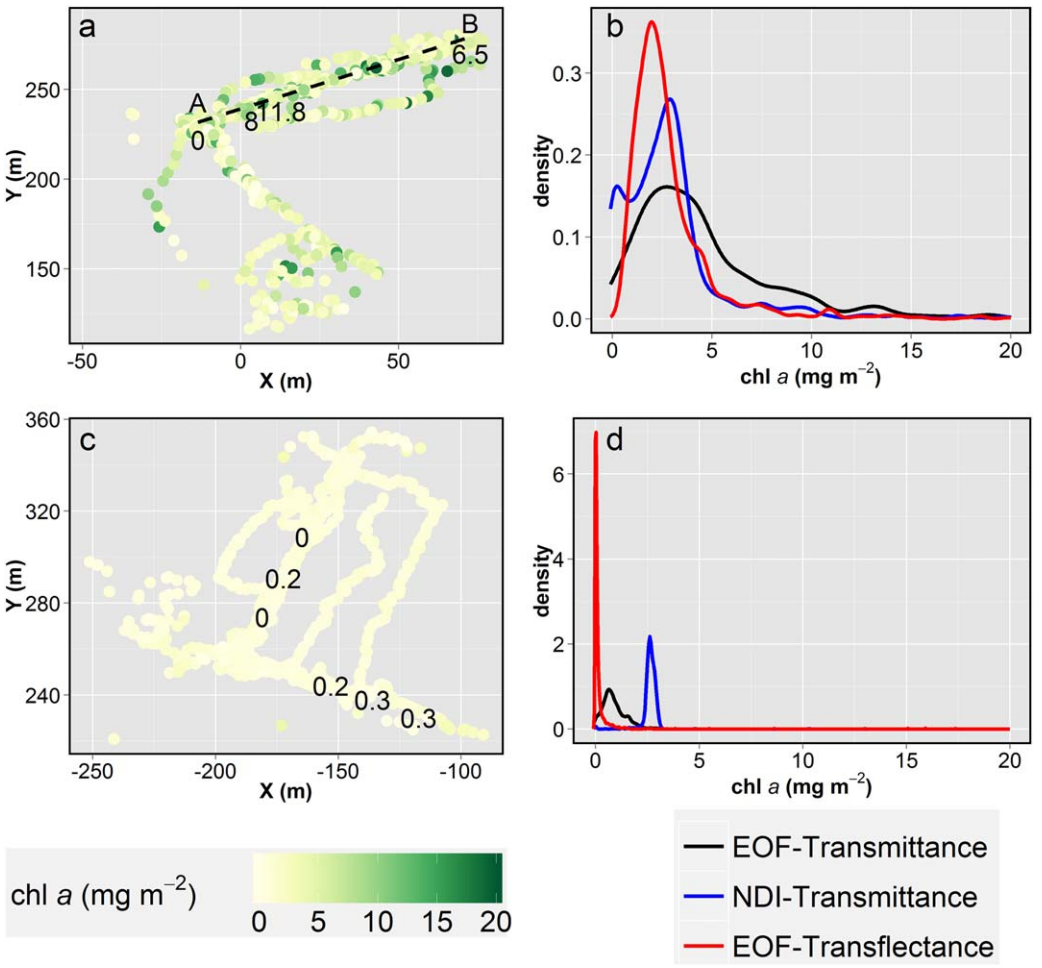

Figure 5. (a and b) Sea ice-algal chl *a* estimates derived from Remotely Operate Vehicle (ROV) under-ice spectral radiation measurements conducted at high-latitude station PS80/360; and (c and d) at low-latitude station PS80/323. (a and c) The spatial distribution of EOF-Transmittance model chl *a* estimates with numerical values of the ice core chl *a* concentrations overlaid at corresponding grid locations. Positions in Figures 5a and 5c are given in a floe fixed coordinate system relative to the ship's GPS receiver. Transect-AB is depicted in Figure 5a by a dashed line. (b and c) Weighted (based on point footprint size) density distributions of estimated chl *a* from the top three predictive models EOF-Transmittance, EOF-Transflectance, and NDI-Transmittance.

Transflectance (*All* data subset, $N = 50$) predictive model and the NDI_{670}-Transmittance (hereafter referred to as NDI-Transmittance, $N = 15$) predictive model for further analyses and comparison. These three predictive models were applied to spectral data collected during two ROV stations (PS80/360 high-latitude site; PS80/323 lower-latitude site) and two SUIT stations (PS80/358 high-latitude site; PS80/285 lower-latitude site).

At the high-latitude ROV and SUIT stations (PS80/360 and 345), the NDI-Transmittance predicted values were, in general, comparable with EOF-Transmittance and EOF-Transflectance predicted values in terms of the location of the density distribution peaks (e.g., modes in Figures 5b and 6b), and median and range of values (Table 5). However, the NDI-Transmittance predicted values had low variability within and between all SUIT and ROV stations in comparison to the EOF-based predicted models and ice core chl *a* values (Table 5 and Figures 5b, 5d, 6b, 6d). At the low-latitude SUIT (PS80/285) and ROV (PS80/323) stations it was apparent that the NDI-Transmittance predictive model over-estimated low-chl *a* values compared to the EOF-based predictive models. This was particularly evident from the substantially higher values observed within chl *a* density distributions for the NDI-Transmittance predicted values compared to EOF-based predicted values (Figures 5d and 6d). Furthermore, there was a large difference between the low-latitude station summaries of NDI-Transmittance predicted chl *a* values and ice core chl *a* concentrations (Table 5). Since the over-estimation of low-chl *a* values and low variability appears to be a constant feature of the NDI-

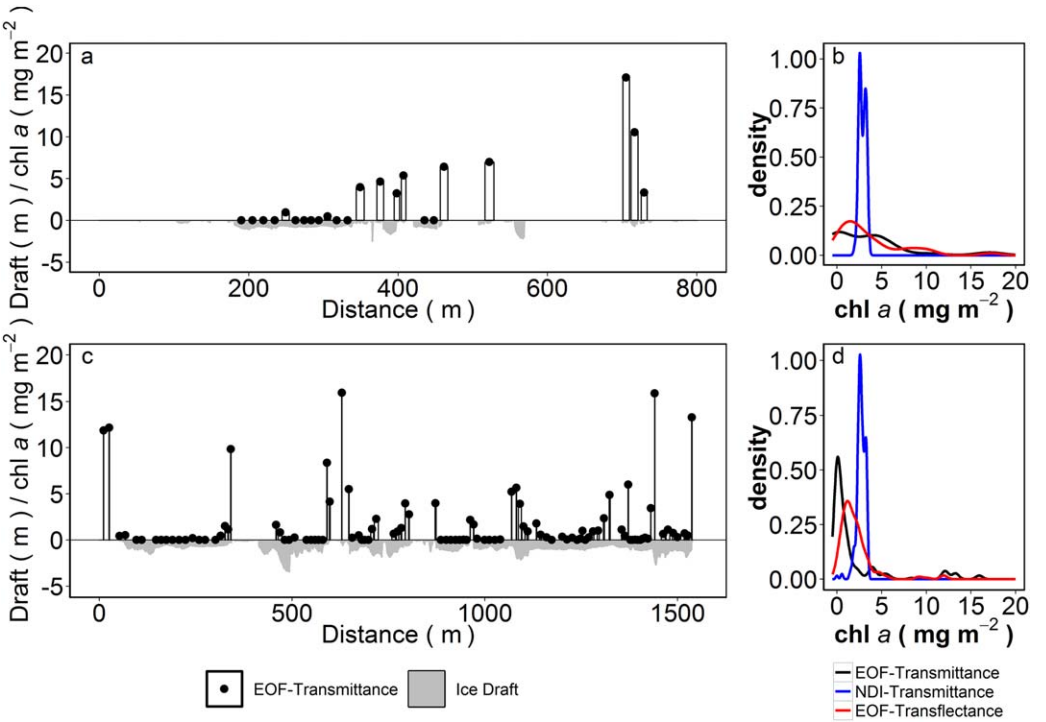

Figure 6. (a and b) Surface and Under-Ice Trawl (SUIT) spectral radiation-derived sea ice-algal chl *a* estimates for high-latitude station PS80/345; and (c and d) for low-latitude station PS80/285. (a and c) The horizontal profile of the EOF-Transmittance model chl a estimates and sea ice draft over the trawled distance, values >0 correspond to chl a (mg m^{-2}) and values <0 correspond to draft (m). The horizontal widths of the bars in Figure 6a and 6c depict relative along-track footprint size. Note the difference in trawled distance in Figures 6a and 6c. (b and c) Weighted (based on point footprint size) density distributions of estimated chl a from the top three predictive models EOF-Transmittance, EOF-Transflectance, and NDI-Transmittance.

Transmittance predictive model, we suggest it was a less reliable predictive model compared to the EOF-based predictive models when applied to larger-scale independent spectral data. Although uncertainty is also high for low-chl *a* values for the EOF-Transmittance and EOF-Transflectance models, the biases are low (almost zero) and therefore over larger-scales should result in minimal over-estimation/under-estimation biases of ice-algal chl *a*. The EOF-based predictive models both showed comparable median and range of chl *a* values at the same stations (Table 5). Hence, both EOF-based models showed similar regional differences in chl *a* concentrations with higher values at the higher latitude stations (Table 5), which is also in agreement with the general trend of our ice core chl *a* concentrations. Overall, however, there was little correlation between the EOF-Transmittance and EOF-Transflectance predictive models' estimated chl *a* values.

Table 5. Summary of Ice Core chl *a* and chl *a* Estimates Derived From Under-Ice Spectral Radiation at the Selected Under-Ice Horizontal Profiling Platform Stations[a]

Region	Platform-Station	Distance, Spacing (m)[b]	Footprint (m^2)[c]	Core chl *a* (mg m^{-2})	EOF-Transmittance Predicted chl *a* (mg m^{-2})	EOF-Transflectance Predicted chl *a* (mg m^{-2})	NDI-Transmittance Predicted chl *a* (mg m^{-2})
High-latitude	ROV-PS80/360	180, 0.9	3.0/0.02	7.25 (4.86–8.99) [4]	3.7 (2.1–5.9) [821]	2.3 (1.6–3.3) [960]	2.6 (1.2–3.5) [927]
	SUIT-PS80/345	625, 24	3.5/0.11		3.2 (0.0–5.0) [23]	2.1 (1.1–4.9) [26]	3.0 (2.6–3.3) [34]
Low-latitude	ROV-PS80/323	180, 0.5	2.6/0.02	0.17 (0.06 – 0.23) [6]	0.8 (0.5–1.1) [1568]	0.01 (0.00–0.11) [1667]	2.7 (2.5–2.8) [1569]
	SUIT-PS80/285	1500, 14	1.6/0.05		0.4 (0.0–1.5) [102]	1.6 (0.9–2.5) [110]	2.7 (2.5–3.0) [118]

[a]ROV: Remotely Operated Vehicle; and SUIT: Surface and Uunder-Ice Trawl. Ice core and predicted chl a values represent the median (50th percentile), interquartile range (25th–75th percentiles), and sample size [*N*].

[b]Distance refers to the distance covered by the profiling platform (e.g., maximum distance between any two points); spacing is the mean spacing between all adjacent points.

[c]Footprint is the mean of all point footprints for Transmittance/Transflectance, respectively.

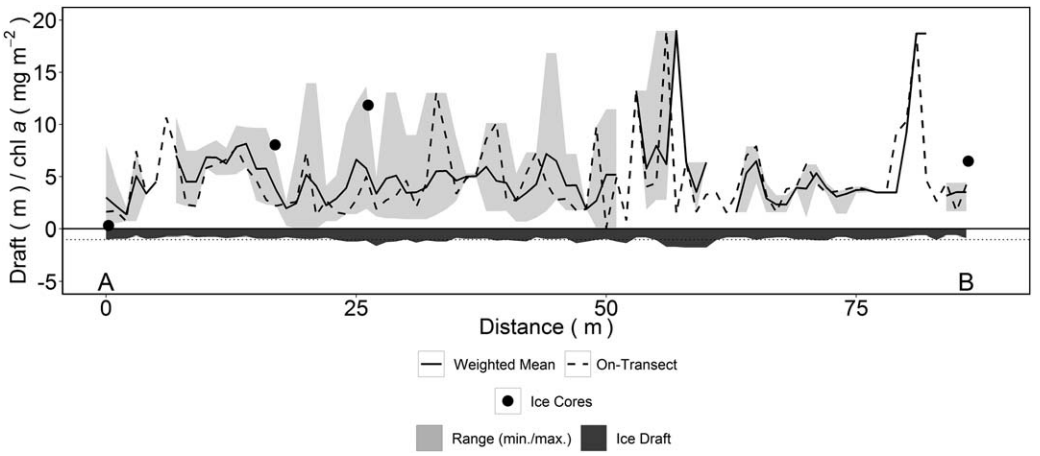

Figure 7. Sea ice-algal chl *a* concentrations along Transect-AB (depicted in Figure 6) extracted from ROV station PS80/360. Shown are ice draft (m), ice core chl *a* values (points) at corresponding locations along the transect, and EOF-Transmittance predictive model chl *a* estimates along the transect. Model predicted chl *a* values correspond to: exactly on the transect (on-transect), and weighted (based on footprint size) mean and range of values within 1.5 m of the transect. *Y* axis values >0 correspond to chl *a* (mg m^{-2}) and values below zero correspond to draft (m). Stippled horizontal line depicts draft of -1 m.

This can be explained by their different mean footprint size, which was 1.5 m for the irradiance sensor, and 0.15 m for the radiance sensor.

In order to account for ROV position uncertainty and the variable footprint size of spectral measurements when comparing independent spectral radiation-derived chl *a* to ice core chl *a* concentrations, we took the weighted (based on footprint of each spectral measurement) mean of all bio-optical chl *a* estimates that were within 1.5 m of each 1 m bin along an 85 m transect (transect-AB Figures 5a and 7). Points within two adjacent overlapping bin areas were assigned to only the closest bin location. Transect-AB includes four ice core sample locations, with the ice core chl *a* concentration values overlaid on the ROV measurement grids (Figures 5a and 5c). The first three ice core chl *a* observations were within the range of values predicted by the EOF-Transmittance model, for the 1.5 m region surrounding the core locations. The estimated chl *a* value at the end of the transect (~85 m), however, was lower than the corresponding ice core value, but still within the model uncertainty ($RMSE_{CV}$ of 1.8 mg chl *a* m^{-2}; Figure 7). The EOF-Transmittance model showed a better fit to the ice core chl *a* observations compared to the EOF-Transflectance and NDI-Transmittance predictive models, which further confirms that the EOF-Transmittance model performs best as a predictive model also indicated by the final model ranking.

A tentative assessment of the spatial variability of ice-algal chl *a* concentrations indicates that large-scale estimates of ice-algal biomass and primary production are sensitive to the choice and number of ice cores analyzed compared to continuous spectral profiles, which capture the variability of ice-algal chl *a* concentrations over larger distances. Based on the up-scaled (SUIT and ROV) EOF-Transmittance predictive model results (Figures 5a, 5c, 6a, and 6c) and the extracted 85 m transect-AB from the ROV station PS80/360 (Figure 7) it is apparent that ice algae biomass has a patchy distribution, which is well-known. Regardless of the patchy distribution, Arctic-wide sea ice primary production estimates, which integrated standing stock chl *a* biomass, used only one to three core samples per location [e.g., *Fernández-Méndez et al*., 2015; *Gosselin et al*., 1997]. The four bio-optical cores sampled along transect AB had an average chl *a* concentration of 6.6 mg m^{-2}. The range of the four cores (~0 to 12 mg chl *a* m^{-2}), however, indicates that basing large-scale estimates on a small number of ice cores carries large uncertainties in biomass and subsequent derived primary production estimates. Based on one ice core sample with an ice-algal biomass of 8 mg chl *a* m^{-2}, *Fernández-Méndez et al*. [2015] estimated that ice algae contributed up to 60% of the total primary production at ice station PS80/360. Along transect AB chl *a* concentrations of sea ice estimated by our most reliable bio-optical predictive model (EOF-Transmittance; Figure 7a) yielded a considerably lower weighted median and interquartile range of 4.0 (2.8–6.4) mg chl *a* m^{-2}, which was also evident from the full ROV survey values for that site (Table 5). A potential difference of over 50% between ROV spectral radiation-derived chl *a* concentration estimates compared to published chl *a* values based on ice core measurements at the

same location emphasizes the importance of high-resolution measurements to capture the spatial variability of ice-algal biomass for large-scale biomass and primary production estimates. In order to conduct detailed spatial analyses of ice-algal biomass chl *a*, however, further geospatial processing of the data is required and is beyond the scope of this study.

4. Conclusions

With this first large-scale bio-optical summer study in the Arctic Ocean, we demonstrated the suitability of different combinations of statistical approaches with four spectral measurements for deriving ice-algal chl *a* concentrations in sea ice, and their application to larger scale spectral measurements. For these late-summer Arctic data, the EOF models performed better than the NDI models, particularly at differentiating between low, medium, and high-chl *a* concentrations. We attributed this to the ability of the EOF models to account for the high variability of environmental properties by incorporating variability from multiple regions of the spectra. Compared to the more complex EOF-based approach, the NDI-based approach may be more easily applied and often suitable, depending on the variability of light conditions, sea ice properties, and sea ice-algal chl *a* concentrations. Regardless of the statistical approach taken, accounting for incoming solar radiation by calculating transmittance and transflectance resulted in superior models compared to simply using under-ice irradiance or radiance. This is particularly important for studies covering large (e.g., ocean basin) spatial and temporal scales, and therefore a wide range of incident light conditions. Considerable discrepancy between mean chl *a* concentrations derived from our most reliable bio-optical model applied to a 85 m spectral transect in comparison to published chl *a* values based on ice core measurements at the same location highlights the need of high-resolution measurements to capture the true variability of ice-algal biomass in the context of large-scale estimates and modeling studies. The increasing use of ROVs and AUVs equipped with spectral sensors means that spectral data for making large-scale chl *a* estimates will become more widespread with continued technological advancements. This study provides a comprehensive analysis of the potentials and limits of predicting chl *a* concentrations in Arctic summer sea ice from spectral data under variable environmental conditions. Furthermore, we presented a detailed methodological approach for studies extending over large spatial and/or temporal scales, using, e.g., autonomous vehicles or moored sea ice observatories.

Acknowledgments
We thank Martin Schiller for his technical expertise and operational support during ROV deployments. We thank Captain Uwe Pahl and Captain Stefan Schwarze, the crews, and scientific cruise leaders Antje Boetius and Ursula Schauer and RV Polarstern expeditions PS80.3 (ARK27-3; IceArc) and PS78.3 (Ark26-3; TransArc), respectively, for their excellent support and guidance with work at sea. We thank Jan Andries van Franeker (IMARES) for kindly providing the Surface and Under-Ice Trawl (SUIT) and Michiel van Dorssen for technical support. SUIT was developed by IMARES with support from the Netherlands Ministry of EZ (project WOT-04-009-036) and the Netherlands Polar Program (project ALW 866.13.009). We acknowledge the collaboration and technical support by Ocean Modules, Sweden for development and deployment of the ROV. Sea ice concentration data from 13 September 2012 were obtained from http://www.meereisportal.de (grant: REKLIM-2013-04). This study is part of the Helmholtz Association Young Investigators Group *Iceflux*: Ice-ecosystem carbon flux in polar oceans (VH-NG-800). We also acknowledge the Alfred-Wegener-Institut, Helmholtz-Zentrum für Polar-und Meeresforschung for essential financial and logistical support. All spectral radiation data are available from the PANGAEA database for PS78 at doi:10.1594/PANGAEA.786717 and for PS80 at doi.pangaea.de/10.1594/PANGAEA.833292.

References

Aguinis, H., R. K. Gottfredson, and H. Joo (2013), Best-Practice recommendations for defining, identifying, and handling outliers, *Organ. Res. Methods*, *16*(2), 270–301, doi:10.1177/1094428112470848.

Arctic Monitoring and Assessment Programme (AMAP) (2011), Snow,water, ice and permafrost in the Arctic (SWIPA): Climate change and the cryosphere, Arctic Monit. and Assess. Programme, Oslo, Norway. [Available at www.amap.no.]

Ambrose, W. G., C. von Quillfeldt, L. M. Clough, P. V. R. Tilney, and T. Tucker (2005), The sub-ice algal community in the Chukchi sea: Large- and small-scale patterns of abundance based on images from a remotely operated vehicle, *Polar Biol.*, *28*(10), 784–795, doi:10.1007/s00300-005-0002-8.

Arrigo, K. R., and G. L. van Dijken (2011), Secular trends in Arctic Ocean net primary production, *J. Geophys. Res.*, *116*, C09011, doi:10.1029/2011JC007151.

Arrigo, K. R., G. van Dijken, and S. Pabi (2008), Impact of a shrinking Arctic ice cover on marine primary production, *Geophys. Res. Lett.*, *35*, L19603, doi:10.1029/2008GL035028.

Boetius, A., et al. (2013), Export of algal biomass from the melting Arctic Sea Ice, *Science*, *339*(6126), 1430–1432, doi:10.1126/science.1231346.

Budge, S. M., M. J. Wooller, A. M. Springer, S. J. Iverson, C. P. McRoy, and G. J. Divoky (2008), Tracing carbon flow in an arctic marine food web using fatty acid-stable isotope analysis, *Oecologia*, *157*(1), 117–129, doi:10.1007/s00442-008-1053-7.

Calcagno, V., and C. de Mazancourt (2010), glmulti: An R package for easy automated model selection with (generalized) linear models, *J. Stat. Software*, *34*(12), 1–29.

Campbell, K., C. J. Mundy, D. G. Barber, and M. Gosselin (2014), Remote estimates of ice algae biomass and their response to environmental conditions during Spring Melt, *Arctic*, *67*(3), 375–387, doi:10.14430/arctic4409.

Campbell, K., C. J. Mundy, D. G. Barber, and M. Gosselin (2015), Characterizing the sea ice algae chlorophyll a—Snow depth relationship over Arctic spring melt using transmitted irradiance, *J. Mar. Syst.*, *147*, 76–84, doi:10.1016/j.jmarsys.2014.01.008.

Cota, G. F., and R. E. H. Smith (1991), Ecology of bottom ice algae. III: Comparative physiology, *J. Mar. Syst.*, *2*(3–4), 297–315.

Craig, S. E., C. T. Jones, W. K. W. Li, G. Lazin, E. Horne, C. Caverhill, and J. J. Cullen (2012), Deriving optical metrics of coastal phytoplankton biomass from ocean colour, *Remote Sens. Environ.*, *119*, 72–83, doi:10.1016/j.rse.2011.12.007.

David, C., B. Lange, B. Rabe, and H. Flores (2015), Community structure of under-ice fauna in the Eurasian central Arctic Ocean in relation to environmental properties of sea-ice habitats, *Mar. Ecol. Prog. Ser.*, *522*, 15–32, doi:10.3354/meps11156.

Fernández-Méndez, M., F. Wenzhöfer, I. Peeken, H. L. Sørensen, R. N. Glud, and A. Boetius (2014), Composition, buoyancy regulation and fate of ice algal aggregates in the Central Arctic Ocean, *PLoS One*, *9*(9), e107452, doi:10.1371/journal.pone.0107452.

Fernández-Méndez, M., C. Katlein, B. Rabe, M. Nicolaus, I. Peeken, K. Bakker, H. Flores, and A. Boetius (2015), Photosynthetic production in the Central Arctic during the record sea-ice minimum in 2012, *Biogeosciences*, *12*, 2897–2945, doi:10.5194/bgd-12-2897-2015.

Fetterer, F., K. Knowles, W. Meier, and M. Savoie (2002, udpated 2011), *Sea Ice Index* [Digital Media], Natl. Snow and Ice Data Cent., Boulder, Colo.
Flores, H., J. A. van Franeker, V. Siegel, M. Haraldsson, V. Strass, E. H. Meesters, U. Bathmann, and W. J. Wolff (2012), The Association of Antarctic Krill *Euphausia superba* with the Under-Ice Habitat, *PLoS One*, *7*(2), e31775, doi:10.1371/journal.pone.0031775.
Gosselin, M., L. Legendre, S. Demers, and R. G. Ingram (1985), Responses of sea-ice microalgae to climatic and fortnightly tidal energy inputs (Manitounuk Sound, Hudson Bay), *Can. J. Fish. Aquat. Sci.*, *42*(5), 999–1006, doi:10.1139/f85-125.
Gosselin, M., L. Legendre, J. C. Therriault, S. Demers, and M. Rochet (1986), Physical control of the horizontal patchiness of sea-ice microalgae, *Mar. Ecol. Prog. Ser.*, *29*(3), 289–298, doi:10.3354/meps029289.
Gosselin, M., L. Legendre, J.-C. Therriault, and S. Demers (1990), Light and nutrient limitation of sea-ice microalgae (Hudson Bay, Canadian Arctic), *J. Phycol.*, *26*(2), 220–232, doi:10.1111/j.0022-3646.1990.00220.x.
Gosselin, M., M. Levasseur, P. A. Wheeler, R. A. Horner, and B. C. Booth (1997), New measurements of phytoplankton and ice algal production in the Arctic Ocean, *Deep Sea Res., Part II*, *44*(8), 1623–1644, doi:10.1016/S0967-0645(97)00054-4.
Grenfell, T. C., and G. A. Maykut (1977), The optical properties of ice and snow in the Arctic Basin, *J. Glaciol.*, *18*(80), 445–463.
Grossi, S., S. Kottmeier, R. Moe, G. Taylor, and C. Sullivan (1987), Sea ice microbial communities. 6: Growth and primary production in bottom ice under graded snow cover, *Mar. Ecol. Prog. Ser.*, *35*(1–2), 153–164.
Gutt, J. (1995), The occurrence of sub-ice algal aggregations off northeast Greenland, *Polar Biol.*, *15*, 247–252, doi:10.1007/BF00239844.
Haas, C., and H. Eicken (2001), Interannual variability of summer sea ice thickness in the Siberian and central Arctic under different atmospheric circulation regimes, *J. Geophys. Res.*, *106*(C3), 4449–4462.
Haas, C., S. Gerland, H. Eicken, and H. Miller (1997), Comparison of sea-ice thickness measurements under summer and winter conditions in the Arctic using a small electromagnetic induction device, *Geophysics*, *62*(3), 749–757, doi:10.1190/1.1444184.
Haas, C., A. Pfaffling, S. Hendricks, L. Rabenstein, J.-L. Etienne, and I. Rigor (2008), Reduced ice thickness in Arctic Transpolar Drift favors rapid ice retreat, *Geophys. Res. Lett.*, *35*, L17501, doi:10.1029/2008GL034457.
Hamre, B., J.-G. Winther, S. Gerland, J. J. Stamnes, and K. Stamnes (2004), Modeled and measured optical transmittance of snow-covered first-year sea ice in Kongsfjorden, Svalbard, *J. Geophys. Res.*, *109*, C10006, doi:10.1029/2003JC001926.
Horner, R., and G. C. Schrader (1982), Relative contributions of ice algae, phytoplankton, and benthic microalgae to primary production in nearshore regions of the Beaufort Sea, *Arctic*, *35*(4), 485–503.
Intergovernmental Panel on Climate Change (IPCC) (2013), Climate change 2013: The physical science basis, in *Contribution of Working Group I to the Fifth Assessment Report of the Intergovernmental Panel on Climate Change*, edited by T. F. Stocker, 1535 pp, Cambridge Univ. Press, Cambridge, U. K.
Järvinen, O., and M. Leppäranta (2011), Transmission of solar radiation through the snow cover on floating ice, *J. Glaciol.*, *57*(205), 861–870, doi:10.3189/002214311798043843.
Katlein, C., M. Fernández-Méndez, F. Wenzhöfer, and M. Nicolaus (2014a), Distribution of algal aggregates under summer sea ice in the Central Arctic, *Polar Biol.*, *38*(5), 719–731, doi:10.1007/s00300-014-1634-3.
Katlein, C., M. Nicolaus, and C. Petrich (2014b), The anisotropic scattering coefficient of sea ice, *J. Geophys. Res.*, *119*, 842–855, doi:10.1002/2013JC009502.
Katlein, C., et al. (2015), Influence of ice thickness and surface properties on light transmission through Arctic sea ice, *J. Geophys. Res. Oceans*, *120*, 5932–5944, doi:10.1002/2015JC010914.
Kohlbach, D., M. Graeve, B. A. Lange, C. David, I. Peeken, and H. Flores (2016), The importance of ice algae-produced carbon in the central Arctic Ocean ecosystem: Food web relationships revealed by lipid and stable isotope analyses, *Limnol. Oceanogr.*, *61*, 2027–2044, doi:10.1002/lno.10351.
Kwok, R., and D. A. Rothrock (2009), Decline in Arctic sea ice thickness from submarine and ICESat records: 1958–2008, *Geophys. Res. Lett.*, *36*, L15501, doi:10.1029/2009GL039035.
Lange, B. A., C. Michel, J. F. Beckers, J. A. Casey, H. Flores, I. Hatam, G. Meisterhans, A. Niemi, and C. Haas (2015), Comparing springtime ice-algal chlorophyll a and physical properties of multi-year and first-year sea ice from the Lincoln Sea, *PLoS One*, *10*(4), e0122418, doi:10.1371/journal.pone.0122418.
Lavoie, D., K. Denman, and C. Michel (2005), Modeling ice algal growth and decline in a seasonally ice-covered region of the Arctic (Resolute Passage, Canadian Archipelago), *J. Geophys. Res.*, *110*, C11009, doi:10.1029/2005JC002922.
Leu, E., C. J. Mundy, P. Assmy, K. Campbell, T. M. Gabrielsen, M. Gosselin, T. Juul-Pedersen, and R. Gradinger (2015), Arctic spring awakening—Steering principles behind the phenology of vernal ice algal blooms, *Prog. Oceanogr.*, *139*, 151–170, doi:10.1016/j.pocean.2015.07.012.
Light, B., T. C. Grenfell, and D. K. Perovich (2008), Transmission and absorption of solar radiation by Arctic sea ice during the melt season, *J. Geophys. Res.*, *113*, C03023, doi:10.1029/2006JC003977.
Mahmood, Z., and S. Khan (2009), On the use of K-Fold cross-validation to choose cutoff values and assess the performance of predictive models in stepwise regression, *Int. J. Biostat.*, *5*(1), Art. 25, doi:10.2202/1557-4679.1105.
Maslanik, J. A., J. C. Stroeve, C. Fowler, and W. Emery (2011), Distribution and trends in Arctic sea ice age through spring 2011, *Geophys. Res. Lett.*, *38*, L13502, doi:10.1029/2011GL047735.
Maykut, G. A., and T. C. Grenfell (1975), Spectral distribution of light beneath 1st-year sea ice in Arctic Ocean, *Limnol. Oceanogr.*, *20*(4), 554–563.
McCullagh, P., and J. A. Nelder (1989), *Generalized Linear Models*, Chapman and Hall, London.
McDonald, S., T. Koulis, J. Ehn, K. Campbell, M. Gosselin, and C. J. Mundy (2015), A functional regression model for predicting optical depth and estimating attenuation coefficients in sea-ice covers near Resolute Passage, Canada, *Ann. Glaciol.*, *56*(69), 147–154, doi:10.3189/2015AoG69A004.
Melbourne-Thomas, J., K. M. Meiners, C. J. Mundy, C. Schallenberg, K. L. Tattersall, and G. S. Dieckmann (2015), Algorithms to estimate Antarctic sea ice algal biomass from under-ice irradiance spectra at regional scales, *Mar. Ecol. Prog. Ser.*, *536*, 107–121, doi:10.3354/meps11396.
Melnikov, I. (1997), *The Arctic Sea Ice Ecosystem*, Gordon and Breach Sci. Publ., Amsterdam.
Melnikov, I. A., E. G. Kolosova, H. E. Welch, and L. S. Zhitina (2002), Sea ice biological communities and nutrient dynamics in the Canada Basin of the Arctic Ocean, *Deep Sea Res., Part I*, *49*(9), 1623–1649, doi:10.1016/S0967-0637(02)00042-0.
Miller, L. A., et al. (2015), Methods for biogeochemical studies of sea ice: The state of the art, caveats, and recommendations, *Elementa: Sci. Anthropocene*, *3*, 000038, doi:10.12952/journal.elementa.000038.
Mundy, C. J., J. K. Ehn, D. G. Barber, and C. Michel (2007), Influence of snow cover and algae on the spectral dependence of transmitted irradiance through Arctic landfast first-year sea ice, *J. Geophys. Res.*, *112*, C03007, doi:10.1029/2006JC003683.

Nicolaus, M., and C. Katlein (2013), Mapping radiation transfer through sea ice using a remotely operated vehicle (ROV), *Cryosphere*, *7*(3), 763–777, doi:10.5194/tc-7-763-2013.
Nicolaus, M., S. Gerland, S. R. Hudson, S. Hanson, J. Haapala, and D. K. Perovich (2010a), Seasonality of spectral albedo and transmittance as observed in the Arctic Transpolar Drift in 2007, *J. Geophys. Res.*, *115*, C11011, doi:10.11029/12009JC006074.
Nicolaus, M., S. R. Hudson, S. Gerland, and K. Munderloh (2010b), A modern concept for autonomous and continuous measurements of spectral albedo and transmittance of sea ice, *Cold Reg. Sci. Technol.*, *62*(1), 14–28, doi:10.1016/j.coldregions.2010.03.001.
Nicolaus, M., C. Katlein, J. Maslanik, and S. Hendricks (2012), Changes in Arctic sea ice result in increasing light transmittance and absorption, *Geophys. Res. Lett.*, *39*, L24501, doi:10.1029/2012GL053738.
Perovich, D. K. (1996), The optical properties of sea ice, *Rep. 96-1*, Cold Reg. Res. and Eng. Lab., Hanover, N. H.
Perovich, D. K., C. S. Roesler, and W. S. Pegau (1998), Variability in Arctic sea ice optical properties, *J. Geophys. Res.*, *103*(C1), 1193–1208, doi:10.1029/97JC01614.
Petrich, C., H. Eicken, C. M. Polashenski, M. Sturm, J. P. Harbeck, D. K. Perovich, and D. C. Finnegan (2012), Snow dunes: A controlling factor of melt pond distribution on Arctic sea ice, *J. Geophys. Res. Oceans*, *117*, C09029, doi:10.1029/2012JC008192.
R-Development-Core-Team (2012), *R: A Language and Environment for Statistical Computing*, R Found. for Stat. Comput., Vienna, Austria.
Rabenstein, L., S. Hendricks, T. Martin, A. Pfaffhuber, and C. Haas (2010), Thickness and surface-properties of different sea-ice regimes within the Arctic Trans Polar Drift: Data from summers 2001, 2004 and 2007, *J. Geophys. Res.*, *115*, C12059, doi:10.1029/2009JC005846.
Riihelä, A., T. Manninen, and V. Laine (2013), Observed changes in the albedo of the Arctic sea-ice zone for the period 1982–2009, *Nat. Clim. Change*, *3*(10), 895–898, doi:10.1038/nclimate1963.
Rintala, J.-M., J. Piiparinen, J. Blomster, M. Majaneva, S. Müller, J. Uusikivi, and R. Autio (2014), Fast direct melting of brackish sea-ice samples results in biologically more accurate results than slow buffered melting, *Polar Biol.*, *37*(12), 1811–1822, doi:10.1007/s00300-014-1563-1.
Rösel, A., and L. Kaleschke (2012), Exceptional melt pond occurrence in the years 2007 and 2011 on the Arctic sea ice revealed from MODIS satellite data, *J. Geophys. Res.*, *117*, C05018, doi:10.1029/2011JC007869.
Rysgaard, S., M. Kühl, R. N. Glud, and J. W. Hansen (2001), Biomass, production and horizontal patchiness of sea ice algae in a high-Arctic fjord (Young Sound, NE Greenland), *Mar. Ecol. Prog. Ser.*, *223*, 15–26, doi:10.3354/meps223015.
Schwarz, G. (1978), Estimating the dimension of a model, *Ann. Stat.*, *6*(2), 461–464, doi:10.1214/aos/1176344136.
Serreze, M. C., M. M. Holland, and J. Stroeve (2007), Perspectives on the Arctic's shrinking sea-ice cover, *Science*, *315*, 1533–1536, doi:10.1126/science.1139426.
Søreide, J. E., M. L. Carroll, H. Hop, W. G. Ambrose, E. N. Hegseth, and S. Falk-Petersen (2013), Sympagic-pelagic-benthic coupling in Arctic and Atlantic waters around Svalbard revealed by stable isotopic and fatty acid tracers, *Mar. Biol. Res.*, *9*(9), 831–850, doi:10.1080/17451000.2013.775457.
Spreen, G., L. Kaleschke, and G. Heygster (2008), Sea ice remote sensing using AMSR-E 89-GHz channels, *J. Geophys. Res.*, *113*, C02S03, doi:10.1029/2005JC003384.
Stroeve, J. C., V. Kattsov, A. Barrett, M. Serreze, T. Pavlova, M. Holland, and W. N. Meier (2012), Trends in Arctic sea ice extent from CMIP5, CMIP3 and observations, *Geophys. Res. Lett.*, *39*, L16502, doi:10.1029/2012GL052676.
Taylor, B. B., M. H. Taylor, T. Dinter, and A. Bracher (2013), Estimation of relative phycoerythrin concentrations from hyperspectral underwater radiance measurements––A statistical approach, *J. Geophys. Res. Oceans*, *118*, 2948–2960, doi:10.1002/jgrc.20201.
Thomas, C. W. (1963), On the transfer of visible radiation through sea ice and snow, *J. Glaciol.*, *4*(34), 481–484.
Tran, S., B. Bonsang, V. Gros, I. Peeken, R. Sarda-Esteve, A. Bernhardt, and S. Belviso (2013), A survey of carbon monoxide and non-methane hydrocarbons in the Arctic Ocean during summer 2010, *Biogeosciences*, *10*(3), 1909–1935, doi:10.5194/bg-10-1909-2013.
Tremblay, J.-É., L. G. Anderson, P. Matrai, P. Coupel, S. Bélanger, C. Michel, and M. Reigstad (2015), Global and regional drivers of nutrient supply, primary production and CO_2 drawdown in the changing Arctic Ocean, *Prog. Oceanogr.*, *139*, 171–196, doi:10.1016/j.pocean.2015.08.009.
van Franeker, J. A., H. Flores, and M. van Dorssen (2009), The surface and under ice trawl (SUIT). Frozen desert alive—The role of sea ice for pelagic macrofauna and its predators, PhD thesis, Univ. of Groningen, Groningen.
Wadhams, P. (2012), The use of autonomous underwater vehicles to map the variability of under-ice topography, *Ocean Dyn.*, *62*(3), 439–447, doi:10.1007/s10236-011-0509-1.
Wang, S. W., S. M. Budge, K. Iken, R. R. Gradinger, A. M. Springer, and M. J. Wooller (2015), Importance of sympagic production to Bering Sea zooplankton as revealed from fatty acid-carbon stable isotope analyses, *Mar. Ecol. Prog. Ser.*, *518*, 31–50, doi:10.3354/meps11076.
Wassmann, P., C. M. Duarte, S. Agusti, and M. K. Sejr (2011), Footprints of climate change in the Arctic marine ecosystem, *Global Change Biol.*, *17*(2), 1235–1249, doi:10.1111/j.1365-2486.2010.02311.x.
Yun, M. S., T. E. Whitledge, D. Stockwell, S. H. Son, J. H. Lee, J. W. Park, D. B. Lee, J. Park, and S. H. Lee (2016), Primary production in the Chukchi Sea with potential effects of freshwater content, *Biogeosciences*, *13*(3), 737–749, doi:10.5194/bg-13-737-2016.